Monthly Notices of the ROYAL ASTRONOMICAL SOCIETY

MNRAS **511,** 3657–3681 (2022) https://doi.org/10.1093/mnras/stac185
Advance Access publication 2022 February 3

The impact of the first galaxies on cosmic dawn and reionization

Julian B. Muñoz [1]★ Yuxiang Qin [2,3] Andrei Mesinger [4] Steven G. Murray [5] Bradley Greig [2,3] and Charlotte Mason [1,6,7]

[1]*Harvard-Smithsonian Center for Astrophysics, 60 Garden St., Cambridge, MA 02138, USA*
[2]*School of Physics, University of Melbourne, Parkville, VIC 3010, Australia*
[3]*ARC Centre of Excellence for All Sky Astrophysics in 3 Dimensions (ASTRO 3D), Parkville, VIC 3010, Australia*
[4]*Scuola Normale Superiore, Pisa, PI I-56126, Italy*
[5]*School of Earth and Space Exploration, Arizona State University, Tempe, AZ 85281, USA*
[6]*Cosmic Dawn Center (DAWN)*
[7]*Niels Bohr Institute, University of Copenhagen, Jagtvej 128, DK-2200 København N, Denmark*

Accepted 2022 January 14. Received 2022 January 13; in original form 2021 November 16

ABSTRACT

The formation of the first galaxies during cosmic dawn and reionization (at redshifts $z = 5$–30), triggered the last major phase transition of our universe, as hydrogen evolved from cold and neutral to hot and ionized. The 21-cm line of neutral hydrogen will soon allow us to map these cosmic milestones and study the galaxies that drove them. To aid in interpreting these observations, we upgrade the publicly available code `21cmFAST`. We introduce a new, flexible parametrization of the additive feedback from: an inhomogeneous, H_2-dissociating (Lyman–Werner; LW) background; and dark matter – baryon relative velocities; which recovers results from recent, small-scale hydrodynamical simulations with both effects. We perform a large, 'best-guess' simulation as the 2021 installment of the Evolution of 21-cm Structure (EOS) project. This improves the previous release with a galaxy model that reproduces the observed UV luminosity functions (UVLFs), and by including a population of molecular-cooling galaxies. The resulting 21-cm global signal and power spectrum are significantly weaker, primarily due to a more rapid evolution of the star formation rate density required to match the UVLFs. Nevertheless, we forecast high signal-to-noise detections for both HERA and the SKA. We demonstrate how the stellar-to-halo mass relation of the unseen, first galaxies can be inferred from the 21-cm evolution. Finally, we show that the spatial modulation of X-ray heating due to relative velocities provides a unique acoustic signature that is detectable at $z \approx 10$–15 in our fiducial model. Ours are the first public simulations with joint inhomogeneous LW and relative-velocity feedback across the entire cosmic dawn and reionization, and we make them available at this link https://scholar.harvard.edu/julianbmunoz/eos-21.

Key words: galaxies: high-redshift – intergalactic medium – cosmology: theory – dark ages, reionization, first stars – diffuse radiation.

1 INTRODUCTION

The epoch of reionization (EoR) and the cosmic dawn (CD) represent fundamental milestones in the history of our universe, and are rapidly becoming the next frontier in astrophysics. These two eras witnessed the last major phase change of our universe, as the intergalactic medium (IGM) evolved from being cold and neutral following recombination, to being hot and ionized due to the radiation emitted by the first galaxies. At present we only hold some pieces of this cosmic puzzle (e.g. Loeb & Furlanetto 2013; Mesinger 2016). Nevertheless, the next few years will see the advent of different observations targeting these cosmic eras (Mellema et al. 2013; Beardsley et al. 2016; DeBoer et al. 2017; Bowman et al. 2018; Greig et al. 2020b; Mertens et al. 2020), which will open a window to the astrophysics of the early universe.

While the stellar content of low-z galaxies is relatively well understood (see e.g. Wechsler & Tinker 2018 for a review), much less is known about the first galaxies that started the CD. Given the hierarchical paradigm of structure formation, we expect the first (Pop III) stars to form in small molecular-cooling galaxies (MCGs) at $z \sim$ 20–30 (Tegmark et al. 1997; Abel, Bryan & Norman 2002; Bromm & Larson 2004; Haiman & Bryan 2006; Trenti 2010), residing in haloes with virial temperatures $T_{\rm vir} \lesssim 10^4$ K (which corresponds to total halo masses $M_{\rm h} \lesssim 10^8\,{\rm M}_\odot$ during the EoR and CD). Feedback eventually quenches star formation in these MCGs, and hierarchical evolution ushers in the era of heavier, atomically cooled galaxies (ACGs; $M_{\rm h} \gtrsim 10^8\,{\rm M}_\odot$). With most ACGs forming out of pre-enriched MCG building blocks, it is likely that second-generation (Pop II) stars drove the bulk of cosmic reionization at $z \sim 5$–10 (e.g. Greig, Mesinger & Bañados 2019; Mason et al. 2019a; Aghanim et al. 2020; Choudhury, Paranjape & Bosman 2021; Qin et al. 2021b).

Current data, from ultraviolet (UV) luminosity functions (UVLFs; Bouwens et al. 2014, 2015, 2021; Atek et al. 2015, 2018; Livermore, Finkelstein & Lotz 2017; Ishigaki et al. 2018; Oesch et al. 2018), the Lyman α forest (Becker et al. 2015; Bosman et al. 2018; Qin et al. 2021b), and the evolution of the volume-averaged hydrogen neutral fraction ($\bar{x}_{\rm HI}$; Mason et al. 2019b; Aghanim et al. 2020), provide some constraints (Park et al. 2019; Naidu et al. 2020) on

★ E-mail: julianmunoz@cfa.harvard.edu

the halo–galaxy connection for ACGs at $z \lesssim 10$. However, very little is known about MCGs or the $z > 10$ universe. The brightest galaxies in this regime will be reached by the James Webb Space Telescope (JWST) and the Nancy Grace Roman Space Telescope (*Roman*). Unfortunately, the bulk of ACGs and MCGs are too faint to be seen with these telescopes, and must be studied indirectly with 21-cm observatories. These include both global-signal efforts like the Experiment to Detect the Global EoR Signature (EDGES), the Shaped Antenna measurement of the background Radio Spectrum (SARAS), the Large-aperture Experiment to Detect the Dark Ages (LEDA), as well as interferometers like the Low-Frequency Array (LOFAR), the Murchison Widefield Array (MWA), the Hydrogen Epoch of Reionization Array (HERA) and the Square Kilometre Array (SKA). Therefore, it is of paramount importance to develop flexible and robust models of the astrophysics of the CD and the EoR to compare against these upcoming data. In this work we build upon the public `21cmFAST` code to include MCGs with all of the relevant sources of feedback.

Stellar formation in MCGs is easily disrupted by different processes, given their shallow potential wells. In addition to feedback from photoheating and supernovae (Draine & Bertoldi 1996; Barkana & Loeb 1999; Wise & Abel 2008; Sobacchi & Mesinger 2013, which also affects stellar formation in ACGs), MCGs suffer from two distinct sources of feedback. The first is driven by Lyman–Werner (LW) radiation, composed of photons in the 11.2–13.6 eV band, which efficiently photodissociate molecular hydrogen (H_2), hampering gas cooling, and subsequent star formation in MCGs (Machacek, Bryan & Abel 2001; Johnson, Greif & Bromm 2007; O'Shea & Norman 2008; Safranek-Shrader et al. 2012; Visbal et al. 2014; Schauer et al. 2017; Skinner & Wise 2020). The second are driven by the dark matter (DM)-baryon streaming velocities (v_{cb}), which impede gas from efficiently accreting and cooling on to DM haloes, thus slowing the formation of the first stars (Tseliakhovich & Hirata 2010; Greif et al. 2011; O'Leary & McQuinn 2012; Naoz, Yoshida & Gnedin 2013; Hirano et al. 2018; Schauer et al. 2019). Until recently it was not clear how these two feedback channels interacted. A clearer picture has emerged from the small-scale hydrodynamical simulations of Pop III star formation in Schauer et al. (2021) and Kulkarni, Visbal & Bryan (2021). In this picture, the two sources of feedback are additive, enhancing the minimum mass that an MCG ought to have to be able to form stars. We synthesize the results from these simulations into a flexible fitting formula that jointly includes both LW and v_{cb} feedback. Along with a calibration for this formula, we assume MCGs host Pop III stars with a simple stellar-to-halo mass relation (SHMR), distinct from that of ACGs hosting Pop II stars.

We include these results into the seminumeric simulation code `21cmFAST`[1] (Mesinger & Furlanetto 2007; Mesinger, Furlanetto & Cen 2011; Murray et al. 2020). This builds upon the implementation of the streaming velocities in `21-cmvFAST` by Muñoz (2019a,b, though in that work it was assumed MCGs and ACGs shared the same SHMR and that LW feedback was isotropic), and the first implementation of MCGs with inhomogeneous LW feedback in `21cmFAST` by Qin et al. (2020a, 2021a, though there relative velocities were not considered and the old LW prescription from Machacek et al. 2001 was used). This code is now able to self-consistently evolve the anisotropic LW background, the streaming velocities, as well as the X-ray, ionizing, and non-ionizing UV backgrounds, necessary to predict the 21-cm signal.

We run a large simulation suite (1.5 Gpc comoving on a side, with 1000^3 cells), as the 2021 installment of the Evolution Of 21-cm Structure (EOS) project, updating those in Mesinger, Greig & Sobacchi (2016). This represents our state of knowledge about cosmic dawn and reionization. We dub this EOS simulation *AllGalaxies*, and we make its most relevant light-cones public.[2] This simulation goes beyond the previous *FaintGalaxies* model, both by including Pop III-hosting MCGs as well as including an SHMR that fits current UVLFs. As a consequence, we predict a slower evolution of the 21-cm signal, and 21-cm fluctuations that are nearly an order of magnitude smaller (see also Mirocha, Furlanetto & Sun 2017; Park et al. 2019). Our *AllGalaxies* (EOS2021) simulation represents the current state-of-knowledge of the evolution of cosmic radiation fields during the first billion years.

Furthermore, we explore how parameters governing star formation and feedback in MCGs impact the 21-cm signal and other observables. We find that MCGs likely dominate the star formation rate density (SFRD) at $z \gtrsim 12$, implying they are important for the timing of the CD but not the EoR (see e.g. Qin et al. 2020a; Wu et al. 2021). We also search for the velocity-induced acoustic oscillations (VAOs) that appear due to the acoustic nature of the streaming velocities (Dalal, Pen & Seljak 2010; McQuinn & O'Leary 2012; Visbal et al. 2012; Fialkov et al. 2013; Muñoz 2019a), and for the first time identify VAOs in a full 21-cm light-cone, as opposed to a co-eval (i.e. fixed-z) box. We predict significant VAOs for redshifts as low as $z = 10$–15, which act as a standard ruler to the cosmic dawn (Muñoz 2019b).

This paper is structured as follows. In Section 2, we introduce our model for the first galaxies, both atomic and molecular cooling, which we use in Section 3 to predict how the epochs of cosmic dawn and reionization unfold. Sections 4 and 5 explore how the first galaxies shape the 21-cm signal, where in the former we vary the MCG parameters in our simulations, and in the latter we study the VAOs. Finally, we conclude in Section 6. In this work we fix the cosmological parameters to the best fit from *Planck* 2018 data (TT, TE, EE + lowE + lensing + BAO in Aghanim et al. 2020), and all distances are comoving unless specified otherwise.

2 MODELLING THE FIRST GALAXIES

We begin by describing our model for the first galaxies. As our seminumerical `21-cmFAST` simulations do not keep track of the metallicity and accretion history of each galaxy, we use population-averaged quantities to relate stellar properties to host halo masses. Although these relations can allow for mixed stellar populations, we will make the simplifying assumption (consistent with simulations and merger-tree models; e.g. Xu et al. 2016a; Mebane, Mirocha & Furlanetto 2018) that on average Pop III stars form in (first generation, unpolluted) MCGs, whereas Pop II stars form in (second generation, polluted) ACGs. ACGs are hosted by haloes with virial temperatures of $T_{\rm vir} \gtrsim 10^4$ K (Oh & Haiman 2002, corresponding to halo masses $M_{\rm h} \gtrsim M_{\rm atom}(z) \sim 10^8\,{\rm M}_\odot$ at the relevant redshifts), whereas MCGs reside in minihaloes with $10^3\ {\rm K} \lesssim T_{\rm vir} \lesssim 10^4$ K (Tegmark & Zaldarriaga 2009, and thus $M_{\rm mol} < M_{\rm h} < M_{\rm atom}$, with $M_{\rm mol}(z) \sim 10^6\,{\rm M}_\odot$ during cosmic dawn). As larger haloes form in the universe, star formation transitions from being dominated by Pop III stars to being dominated by Pop II stars (e.g. Schneider et al. 2002). We now describe how these galaxy populations are modelled and the feedback processes that affect them.

[1]Publicly available at https://github.com/21cmfast/21cmFAST.

[2]EOS light-cones can be downloaded at this link.

2.1 Pop II star formation in atomic-cooling galaxies

For the better-understood Pop II stars forming in ACGs we follow the model from Park et al. (2019), which we now briefly review.

The key ingredient that enters our calculations is the (spatially varying) star formation rate density (SFRD), which for ACGs we calculate as

$$\mathrm{SFRD}^{(\mathrm{II})} = \int \mathrm{d}M_\mathrm{h} \frac{\mathrm{d}n}{\mathrm{d}M_\mathrm{h}} \dot{M}_*^{(\mathrm{II})} f_\mathrm{duty}^{(\mathrm{II})}, \tag{1}$$

where $\mathrm{d}n/\mathrm{d}M_\mathrm{h}$ is the conditional halo mass function (HMF; e.g. Barkana & Loeb 2004), $f_\mathrm{duty}^{(\mathrm{II})}$ is a duty cycle (i.e. halo occupation fraction) described below, and $\dot{M}_*$ is the star formation rate (SFR). The superscripts $^{(\mathrm{II})}$ denote that a quantity refers to Pop II-dominated ACGs.

For both ACGs and MCGs, we assume that the SFR is proportional (on average) to the stellar mass divided by a characteristic time-scale:

$$\dot{M}_*^{(i)} = \frac{M_*^{(i)}}{t_* H^{-1}(z)}, \tag{2}$$

where H is the Hubble expansion rate, and t_* is a free parameter, which for simplicity we fix to $t_* = 0.5$ (as it will be degenerate with the normalization of the stellar fraction).

The SHMR is modelled as a simple power law:

$$M_*^{(\mathrm{II})} = f_{*,10}^{(\mathrm{II})} \frac{\Omega_b}{\Omega_\mathrm{m}} \left(\frac{M_\mathrm{h}}{10^{10}\mathrm{M}_\odot} \right)^{\alpha_*^{(\mathrm{II})}} M_\mathrm{h}, \tag{3}$$

where $\Omega_\mathrm{b/m}$ are the baryon and matter densities. This SHMR is governed by two parameters, the normalization $f_{*,10}^{(\mathrm{II})}$ (defined at a characteristic scale $M_\mathrm{h} = 10^{10}\,\mathrm{M}_\odot$), and a power-law index $\alpha_*^{(\mathrm{II})}$, which controls its mass dependence.[3] The value of this index could be set by supernovae (SNe) feedback, which is thought to regulate star formation inside these small galaxies (e.g. Wyithe & Loeb 2013; Dayal et al. 2014; Yung et al. 2019).

This model, without any additional redshift dependence, provides an excellent fit to current EoR observations at $5 \lesssim z \lesssim 10$, including the Lyman-α forest opacity fluctuations (Qin et al. 2021b) and the faint-end UVLFs (Park et al. 2019; Rudakovskyi et al. 2021) (or the entire luminosity range if a high-mass turnover is added to characterize AGN-induced feedback in rare, bright galaxies; e.g. Sabti, Muñoz & Blas 2021c).

The final part of equation (1) is the duty fraction,

$$f_\mathrm{duty}^{(\mathrm{II})} = \exp\left(-M_\mathrm{turn}^{(\mathrm{II})} / M_\mathrm{h} \right), \tag{4}$$

which accounts for inefficient star formation below a characteristic scale $M_\mathrm{turn}^{(\mathrm{II})}$. Haloes below $M_\mathrm{turn}^{(\mathrm{II})}$ are exponentially less likely to host an ACGs, due to inefficient atomic cooling and/or feedback, as discussed below.

2.1.1 *Feedback on ACGs*

As in previous work (e.g. Qin et al. 2020a), we consider two sources of feedback in ACGs: photoheating and supernovae.

Radiation during cosmic reionization heats the gas around low-mass galaxies (both atomic and molecular cooling), delaying its collapse and subsequent star formation (e.g. Thoul & Weinberg 1996; Noh & McQuinn 2014). We use the 1D collapse-simulation results from Sobacchi & Mesinger (2014) to calculate the (local) critical halo mass below which star formation becomes inefficient due to photoheating (see also Hui & Gnedin 1997; Okamoto, Gao & Theuns 2008; Katz et al. 2020; Ocvirk et al. 2020):

$$\frac{M_\mathrm{crit}^\mathrm{ion}}{2.8\times10^9\mathrm{M}_\odot} = \left(\frac{\Gamma_\mathrm{ion}}{10^{-12}\mathrm{s}^{-1}} \right)^{0.17} \left(\frac{10}{1+z} \right)^{2.1} \left[1 - \left(\frac{1+z}{1+z^\mathrm{ion}} \right)^2 \right]^{2.5}, \tag{5}$$

where Γ_ion is the local ionizing background, and z^ion is the reionization redshift of the simulation cell.

Therefore, for ACGs the turn-over mass is

$$M_\mathrm{turn}^{(\mathrm{II})} = \max\left(M_\mathrm{crit}^\mathrm{ion}, M_\mathrm{atom} \right), \tag{6}$$

where $M_\mathrm{atom} = 3.3 \times 10^7\,\mathrm{M}_\odot [(1+z)/21]^{-3/2}$ during the epoch of interest for our fiducial cosmology.

We additionally include feedback from supernovae (SNe) or radiative processes by assuming a smaller fraction of gas is available to form stars inside smaller-mass haloes. Such 'feedback-limited' models result in a (positive) power-law scaling of the SHMR, c.f. the power-law index $\alpha_*^{(\mathrm{II})}$ introduced in equation (3) (e.g. Wyithe & Loeb 2013). We fix this parameter to $\alpha_*^{(\mathrm{II})} = 0.5$ in this work, as it provides an excellent fit to UV LFs at $z = 6$–10 (Qin et al. 2021b). Different authors infer somewhat different values of $\alpha_*^{(\mathrm{II})}$, as they can depend on the assumed star formation histories (e.g. Tacchella et al. 2018; Behroozi et al. 2019). Although $\alpha_*^{(\mathrm{II})}$ could also evolve with time, $z = 2$–10 LFs are consistent with a constant value (e.g. Mason et al. 2015; Tacchella et al. 2018; Mirocha et al. 2021). Our implementation also allows for the possibility that SNe feedback results in an additional characteristic mass scale [effectively adding M_SNe to the RHS of equation (6); c.f. Qin et al. 2020a]. However, we do not consider that possibility in our fiducial model (setting $M_\mathrm{SNe} < \max[M_\mathrm{crit}^\mathrm{ion}, M_\mathrm{atom}]$); this is supported by $z = 0$ data that seems to show no cutoff for haloes down to $M_\mathrm{h} \approx 10^9\,\mathrm{M}_\odot$ (Nadler et al. 2020) roughly at the M_atom threshold (which however are likely not actively star forming at $z = 0$).

2.2 Pop III star formation in molecular-cooling galaxies

The star formation and feedback mechanisms in the first MCG galaxies are still not fully understood. For simplicity, we will assume their SHMR has the same, generic power law form as ACGs, with a few modifications (see Qin et al. 2020a for further details of the implementation in `21cmFAST`). We take the Pop III SFRD[4] to be

$$\mathrm{SFRD}^{(\mathrm{III})} = \int \mathrm{d}M_\mathrm{h} \frac{\mathrm{d}n}{\mathrm{d}M_\mathrm{h}} \dot{M}_*^{(\mathrm{III})} f_\mathrm{duty}^{(\mathrm{III})}. \tag{7}$$

The changes with respect to equation (1) are in the SFR and the duty cycle. For the former, we assume the same relation between $\dot{M}_*$ and M_* as equation (3), though we allow MCGs to have a unique SHMR:

$$M_*^{(\mathrm{III})} = f_{*,7}^{(\mathrm{III})} \frac{\Omega_\mathrm{b}}{\Omega_\mathrm{m}} \left(\frac{M_\mathrm{h}}{10^7\mathrm{M}_\odot} \right)^{\alpha_*^{(\mathrm{III})}} M_\mathrm{h}, \tag{8}$$

which has two new free parameters, $f_{*,7}^{(\mathrm{III})}$, and $\alpha_*^{(\mathrm{III})}$.

[3] We note that we could rephrase the galaxy–halo connection in terms of $\tilde{f}_* = \dot{M}_*/\dot{M}_\mathrm{h}$ rather than f_*, and assume a halo-accretion rate $\dot{M}_\mathrm{h}$, as in Mason, Trenti & Treu (2015), Tacchella et al. (2018), and Mirocha, La Plante & Liu (2021). For an exponential accretion rate $\dot{M}_\mathrm{h} = M_\mathrm{h}/t_*$ (which provides a good fit to simulations; Schneider, Giri & Mirocha 2021) these two formulations are identical.

[4] We introduce an approximation to analytically calculate the SFRD within `21-cm FAST`. This dramatically speeds up the calculation of the SFRD tables, reducing that computational cost by nearly two orders of magnitude. This option can be turned on by setting `FAST_FCOLL_TABLES = True`. We encourage the reader to visit Appendix B for details.

The other difference is the MCG duty cycle

$$f_{\rm duty}^{\rm (III)} = \exp(-M_{\rm turn}^{\rm (III)}/M_{\rm h})\exp(-M_{\rm h}/M_{\rm atom}), \quad (9)$$

which follows our previous assumption that there is a smooth transition from MCGs (below $M_{\rm atom}$) forming Pop III stars to ACGs (above that mass) forming Pop II stars. Further, there is a lower mass cutoff $M_{\rm turn}^{\rm (III)}$ for MCG stellar formation, set by different feedback processes as detailed below. *Our comprehensive treatment of* $M_{\rm turn}^{\rm (III)}$ *represents the main modelling improvement of this work.*

2.1.1 Feedback on MCGs

MCGs reside in haloes with shallow gravitational potentials, which makes them highly sensitive to different effects that disrupt their gas distribution, abundance, or H_2 content. In addition to the previously mentioned feedback, MCGs are also sensitive to: (i) Lyman–Werner photons, and (ii) the DM-baryon relative velocities. As we did for ACGs, we set the turnover mass to be

$$M_{\rm turn}^{\rm (III)} = \max\left(M_{\rm crit}^{\rm ion}, M_{\rm mol}\right), \quad (10)$$

where the first term accounts for photoionization feedback, and the second accounts for the additional impact of LW and $v_{\rm cb}$.

Both the LW and $v_{\rm cb}$ feedback effects impede stellar formation, and the simulations from Schauer et al. (2021) and Kulkarni et al. (2021) show that their joint impact is cumulative. We model the molecular-cooling turnover mass as a product of three factors:

$$M_{\rm mol} = M_0(z)\, f_{v_{\rm cb}}(v_{\rm cb})\, f_{\rm LW}(J_{21}), \quad (11)$$

where J_{21} is the LW intensity in units of 10^{-21} erg s^{-1} cm^{-2} Hz^{-1} sr^{-1}, and $M_0(z) = \tilde{M}_0 \times (1+z)^{-3/2}$ is the (no-feedback) molecular-cooling threshold, with $\tilde{M}_0 = 3.3 \times 10^7 {\rm M}_\odot$ (corresponding to $T_{\rm vir} = 10^3$ K; Tegmark et al. 1997). The two factors $f_{\rm LW}$ and $f_{v_{\rm cb}}$ encode the two new sources of feedback, and our chosen functional form assumes that they add coherently (as assumed previously in Fialkov et al. 2013 and Muñoz 2019a) and are redshift independent. This was shown to be the case in Schauer et al. (2021) for values of $J_{21} \leq 0.1$, as well as in Kulkarni et al. (2021) for $J_{21} = 1$. For larger values, $J_{21} \geq 10$, however, the simulations of Kulkarni et al. (2021) show a deviation from this form (towards less suppression). This large-J_{21} regime only occurs at $z \lesssim 6$ in our simulations, at which point ACGs completely dominate the global SFRD, making MCGs (and thus their feedback mechanisms) largely irrelevant when computing radiation backgrounds.

2.2.2 Lyman–Werner feedback

Photons in the LW band (11.2–13.6 eV) can photodissociate H_2 molecules, thus impeding the ability of gas to cool on to MCGs (Tegmark et al. 1997; Abel et al. 2002; Bromm & Larson 2004; Haiman & Bryan 2006; Trenti 2010). Machacek et al. (2001) showed that the minimum halo mass for star formation in MCGs has a power-law dependence on J_{21}. This result has been the standard in studies of CD and the EoR (see e.g. Fialkov et al. 2013; Visbal et al. 2014; Mirocha et al. 2018; Muñoz 2019a; Qin et al. 2021a, 2020a). However, recent simulations have shown that self-shielding can be important, which reduces the suppression produced by a given LW background. We include these improved results in our analysis.

In particular, we use the results from Kulkarni et al. (2021) and Schauer et al. (2021, see also Skinner & Wise 2020 for similar conclusions), which have independently tackled the issue of jointly simulating the effects of LW (including self-shielding) and relative-velocity feedback (which we will explore later) on the first stars. From equation (11) we can separate the LW feedback factor

$$f_{\rm LW} = \frac{M_{\rm mol}(J_{21})}{M_{\rm mol}(0)}, \quad (12)$$

and calculate it from simulation results, which factors out differences in the zero-point mass (i.e. on the mass M_0 in the absence of feedback). We show the simulation results for $f_{\rm LW}$ in Fig. 1, where it is clear that the Kulkarni et al. (2021) results are below the Schauer et al. (2021) ones, even for larger values of J_{21}. However, a direct comparison of their results is difficult due to differences in the assumed LW intensities: Kulkarni et al. (2021) considered $J_{21} \geq 1$ (or zero), whereas Schauer et al. (2021) considered $J_{21} \leq 0.1$.

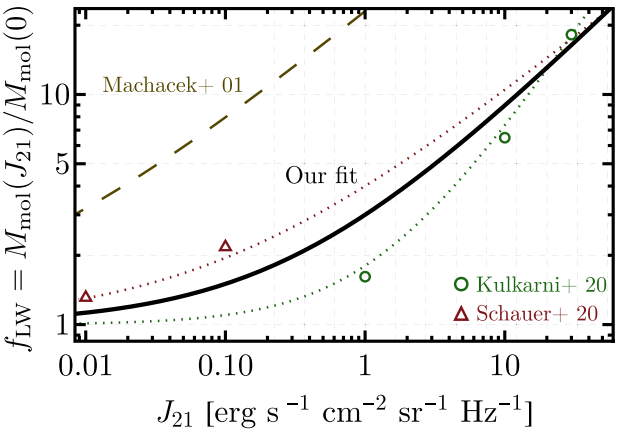

Figure 1. Feedback factor $f_{\rm LW}$ describing how the turnover (minimum) mass for a molecular-cooling halo to form stars grows due to LW feedback, as a function of the LW intensity J_{21} in units of 10^{-21} erg s^{-1} cm^{-2} sr^{-1} Hz^{-1}. The data points are reduced from simulation data in Kulkarni et al. (2021, green) and Schauer et al. (2021, red). Our fit, which sits in the middle in solid black, follows equation (13) with $A_{\rm LW} = 2$ and $\beta_{\rm LW} = 0.5$. The parameters of equation (13) can be modified to closely follow each simulation, as the red and green lines are obtained with different parameter combinations. The dashed brown line is the fit from Machacek et al. (2001), which did not include self-shielding.

Rather than use a fit to $f_{\rm LW}$ from either group, we use a flexible parametrization inspired by Visbal et al. (2014):

$$f_{\rm LW} = 1 + A_{\rm LW}(J_{21})^{\beta_{\rm LW}}, \quad (13)$$

with $A_{\rm LW}$ and $\beta_{\rm LW}$ as free parameters that can be varied within `21cmFAST`. The Kulkarni et al. (2021) simulation results can be well fit setting $\{A_{\rm LW}, \beta_{\rm LW}\} = \{0.8, 0.9\}$, whereas the Schauer et al. (2021) ones require $\{A_{\rm LW}, \beta_{\rm LW}\} = \{3.0, 0.5\}$, which indicates stronger feedback, though a weaker dependence with J_{21}. Both of these fits are shown in Fig. 1. Instead of choosing between these two, we use the flexibility of equation (13) to propose a joint fit, which lands in between both simulation results, with $A_{\rm LW} = 2$ and $\beta_{\rm LW} = 0.6$ (where the round numbers are purposefully chosen to avoid conveying more agreement than the simulations provide). These will be our fiducial parameters for this work. For reference, the old work of Machacek et al. (2001), which did not account for self-shielding, had $\{A_{\rm LW}, \beta_{\rm LW}\} = \{22, 0.47\}$, producing a correction that was nearly a factor of 10 larger (also shown in Fig. 1). We emphasize that we assume that the LW feedback factor only depends on J_{21}, and not on z or any halo property, as a simplifying assumption, which could however be revisited if required by further simulations.

2.2.3 *Relative-velocity feedback*

The DM-baryon relative velocities impede the formation of stars in the first galaxies in two main ways. The first one, pointed out in Tseliakhovich & Hirata (2010, see also Naoz, Yoshida & Gnedin 2012), is that regions of large velocity show suppressed matter fluctuations at small scales, as the baryons there contribute less to the growth of structure. As a consequence, the abundance of small-mass haloes is modulated by relative velocities: fewer collapsed haloes reside in regions with large streaming motions. This effect is difficult to include in our seminumerical simulations, as it would require altering the power spectrum at each cell.[5] Instead, we include this effect on average by modifying the power spectrum in all cells. We solve for the evolution of the baryon and DM overdensities following Muñoz (2019a, based on Tseliakhovich & Hirata 2010), and find that the impact of $v_{\rm bc}$ on the power spectrum at a wavenumber k is well captured by

$$\frac{P_{\rm m}(k,z;v_{\rm cb})}{P_{\rm m}(k,z;0)} = 1 - A_{\rm p}\exp\left[-\frac{(\log[k/k_{\rm p}])^2}{2\sigma_{\rm p}^2},\right] \quad (14)$$

where the three free parameters, A_p, k_p, and σ_p depend on $v_{\rm cb}$, and mildly on z. Here, we fix to the values at $z = 20$ and at the root mean square (rms) relative velocity ($v_{\rm cb} = v_{\rm rms}$), which are $A_p = 0.24$, $k_{\rm p} = 300\,{\rm Mpc}^{-1}$, and $\sigma_p = 0.9$. This is conservative, in that it will yield no VAOs (as these quantities do not spatially fluctuate) and will suppress MCGs by roughly the average amount. We encourage the interested reader to visit Appendix A for details of how this fit is obtained, as well as to find the fit as a function of z and $v_{\rm cb}$. This matter-fluctuation suppression also affects ACGs, and therefore should be included even when MCGs are not. However, we find this to be a subdominant effect to the one we will discuss next, and thus our average treatment will suffice. We leave for future work implementing the fluctuations on this suppression.

The second – and largest – effect of the velocities is to suppress star formation in MCGs (Dalal et al. 2010; Tseliakhovich, Barkana & Hirata 2011). Small haloes in regions with large relative velocities have difficulties in accreting gas, as well as cooling gas into stars (e.g. Greif et al. 2011; Naoz et al. 2013; Schauer et al. 2019).

The small-scale (∼Mpc) hydrosimulations of Schauer et al. (2021) and Kulkarni et al. (2021) were the first to investigate the impact of streaming velocities together with LW feedback. Both groups account for the relative velocities in a similar fashion, and solve for the evolution of gas inside MCGs to find if the conditions for star formation are met. Both works find that the streaming motions impede star formation in the smallest galaxies, raising the minimum mass $M_{\rm mol}$ required for star formation (in the absence of photoheating feedback). Analogously to $f_{\rm LW}$, we define a feedback factor also for $v_{\rm cb}$:

$$f_{v_{\rm cb}} = \frac{M_{\rm mol}(v_{\rm cb})}{M_{\rm mol}(0)}. \quad (15)$$

We calculate this factor for the different simulation outputs of the two groups, and plot it in Fig. 2, which shows the excellent agreement between the two simulation suites.

[5]We note that the relative velocities are coherent on scales below 3 Mpc (Tseliakhovich & Hirata 2010), and thus can be taken to be constant within each of our cells.

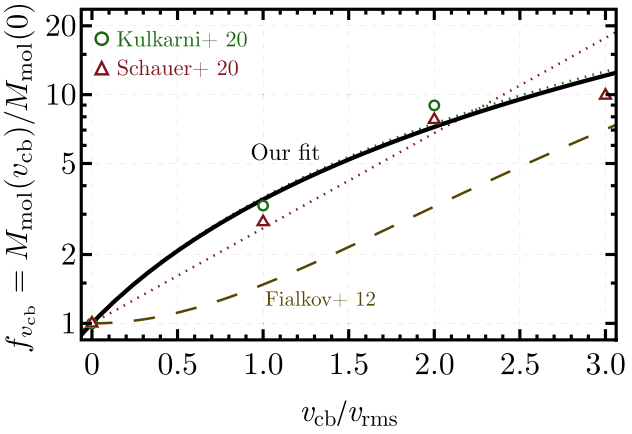

Figure 2. Same as Fig. 1 but for the DM-baryon relative velocity $v_{\rm cb}$ (here divided by its rms value $v_{\rm rms}$ so it is dimensionless). Our fit, in solid black, follows equation (16), and the red and green lines show the fits from each of the two references. The brown dashed line shows the formula from Fialkov et al. (2012), which underpredicts the star formation suppression from relative velocities.

We fit $f_{v_{\rm cb}}$ as a z-independent function, following the functional form in Kulkarni et al. (2021):

$$f_{v_{\rm cb}} = \left(1 + A_{v_{\rm cb}}\frac{v_{\rm cb}}{v_{\rm rms}}\right)^{\beta_{v_{\rm cb}}}, \quad (16)$$

where $v_{\rm rms} \approx 30\,{\rm km\,s^{-1}}$ is the rms velocity, and we use $A_{v_{\rm cb}} = 1$, and $\beta_{v_{\rm cb}} = 1.8$, very similar to the values in Kulkarni et al. (2021). We compare this fit with the previous formula from Fialkov et al. (2012), where it was assumed that the halo virial velocity at the suppression scale follows:

$$V_{\rm mol} = \left[V_0^2 + \alpha_{\rm cb}^2 {v_{\rm cb}}^2(z)\right]^{1/2}, \quad (17)$$

where $V_0 = 4\,{\rm km\,s^{-1}}$ is the virial velocity of molecular-cooling haloes in the absence of any feedback, and they find $\alpha_{\rm cb} = 4$. This translates into a scaling $f_{v_{\rm cb}} = (V_{\rm mol}(v_{\rm cb})/V_0)^3$, shown in Fig. 2, which underpredicts the impact of the relative velocities by roughly a factor of 2.

With a prescription for both sources of feedback, we can evaluate $M_{\rm mol}$ in equation (11). We show this turnover mass at $z = 20$ in Fig. 3 for different values of $v_{\rm cb}$ (in units of its rms value $v_{\rm rms}$, which is close to its median) and J_{21} (we mark the values expected at $z = 20$ for two of our fiducial parameter sets: EOS and OPT, see Table 1). We predict $M_{\rm mol} \approx 10^6\,{\rm M}_\odot$ at $z = 20$, though clearly this quantity depends strongly on $v_{\rm cb}$. This dependence will imprint $M_{\rm mol}$ – and thus the SFRD – with the fluctuations of $v_{\rm cb}$, giving rise to velocity-induced acoustic oscillations, which we study in Section 5.

We find that $M_{\rm mol}$ depends less strongly on J_{21}. In particular, for $J_{21} < 10^{-1}$ the effect of LW feedback is rather weak, and $v_{\rm cb}$ feedback dominates. The situation is reversed for $J_{21} > 10^{0.5}$, though we caution that the two feedback schemes may not add coherently in such a high LW flux regime (Kulkarni et al. 2021). Luckily, this regime does not have a large impact on observables, as it produces $M_{\rm mol} \approx M_{\rm atom}$, so Pop III star formation in MCGs would be subdominant compared to Pop II in ACGs. Moreover, as we will see, values of $J_{21} > 10^{0.5}$ only appear at very late times ($z \lesssim 10$) in our simulations, where Pop II star formation far dominates.

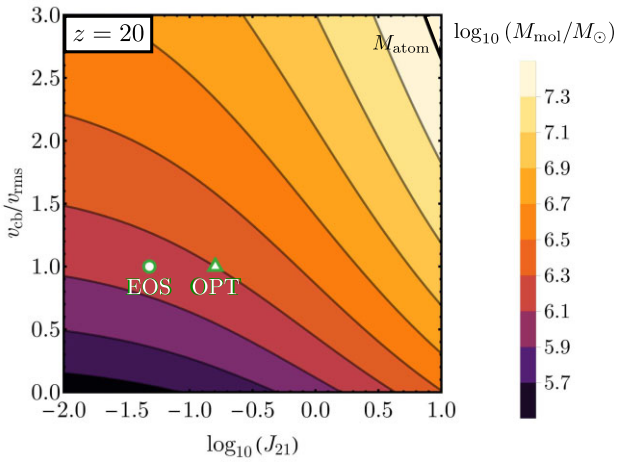

Figure 3. Value of the minimum-mass $M_{\rm mol}$ for a molecular-cooling halo to host Pop III stellar formation at $z = 20$, as a function of the LW flux (J_{21} in the customary units of 10^{-21} erg s^{-1} Hz^{-1} cm^{-2} sr^{-1}) and the streaming velocity ($v_{\rm cb}$ divided by its rms value $v_{\rm rms}$), following equation (11). We assume negligible photoionization feedback at this redshift. Marked green points represent the expected fluxes J_{21} for our two fiducial simulation sets presented in Table 1. The black solid line shows $M_{\rm atom}$, above where there is no Pop III stellar formation (see Section 2.2).

Table 1. Summary of our choices for some of the main free parameters related to the SFRD (top part), ionizations (middle), and X-ray emission (bottom). The EOS 2021 (EOS) fiducial model is used throughout the text, except in the last two sections (4 and 5) where we use OPT. Other parameters are fixed to the values motivated in the text.

Parameter	Fiducial (EOS2021)	Optimistic (OPT)
$\log_{10} f_{*,10}^{\rm (II)}$	-1.25	-1.50
$\log_{10} f_{*,7}^{\rm (III)}$	-2.5	-1.75
$\alpha_*^{\rm (II)}$	0.5	0.5
$\alpha_*^{\rm (III)}$	0	0
$\log_{10} f_{\rm esc,10}^{\rm (II)}$	-1.35	-1.20
$\log_{10} f_{\rm esc,7}^{\rm (III)}$	-1.35	-2.25
$\alpha_{\rm esc}^{\rm (II)} = \alpha_{\rm esc}^{\rm (III)}$	-0.3	-0.3
$L_X^{\rm (II)} = L_X^{\rm (III)}$	40.5	40.5
E_0 [keV]	0.5	0.2

2.3 Comparison: Pop II versus Pop III

Armed with our two stellar populations (Pop II residing in ACGs, and Pop III in MCGs), and the feedback processes that can affect them (LW and relative velocities for MCGs, and stellar and photoheating feedback for both), we can now compare their relative contribution to different cosmic epochs.

We choose a set of fiducial parameters, which we dub EOS (later in Sections 4 and 5 we will study parameter variations), where the stellar fractions of ACGs and MCGs are set to

$$\log_{10} f_{*,10}^{\rm (II)} = -1.25$$

$$\log_{10} f_{*,7}^{\rm (III)} = -2.5,$$

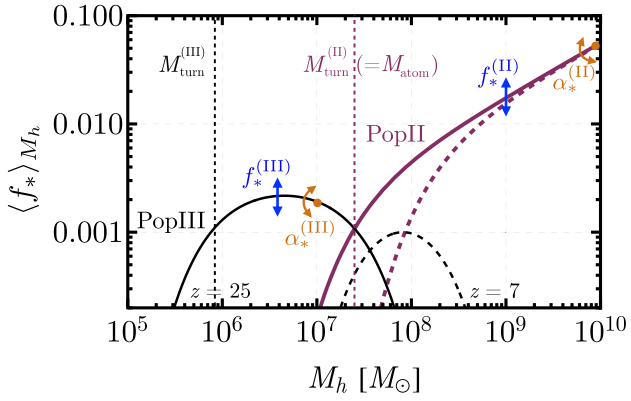

Figure 4. The fraction of galactic mass in stars, averaged over all haloes of a given mass, $\langle f_* \rangle_{M_{\rm h}}$, for our fiducial (EOS2021) simulation. In thick purple lines, we show our model for Pop II-forming ACGs and in thin black lines for Pop III-forming MCGs. The solid lines show this SHMR $\langle f_* \rangle_{M_{\rm h}}$ during cosmic dawn ($z = 25$), whereas dashed are at the EoR ($z = 7$). Vertical dotted lines represent the turnover mass to form stars for MCGs (black, including feedback) and for ACGs (purple), both at $z = 25$. Both SHMRs are parametrized via power laws with indices α_*^i, which vary the tilt as indicated by the orange arrows, and amplitudes f_*^i, which scale them up and down as per the blue arrows. This relation is expected to turn over at much higher masses ($M_{\rm h} \gtrsim 10^{11}$–$10^{12}\,{\rm M}_\odot$), which we do not consider as such objects are too rare to appreciably contribute to cosmic radiation fields during these eras.

with SHMR power-law indices given by

$$\alpha_*^{\rm (II)} = 0.5$$

$$\alpha_*^{\rm (III)} = 0.$$

The ACG parameters are very similar to the maximum a posteriori (MAP) from Qin et al. (2021b), which reproduces observations of the UVLFs, the cosmic-microwave background (CMB) optical depth, and the high-z Lyman α forest opacity fluctuations. Our choice of $\log_{10} f_{*,7}^{\rm (III)} = -2.5$ is rather conservative (though slightly larger than found in the simulations of Skinner & Wise 2020), but it still allows Pop III stars to dominate the SFRD at early enough times. Given that the Pop III parameters are entirely unknown, we will focus on varying the latter in this work, though we note that the `21cmMC` (Greig & Mesinger 2015) [6] and `21cmFish` (Mason, Munoz & Others)[7] packages allow the user to vary all parameters simultaneously.

We begin by showing the SHMR ($f_* = M_*/M_{\rm h}$) of Pop II- and Pop III-hosting galaxies in Fig. 4 at $z = 25$ and 7. The impact of the four free parameters is as follows: each index α_*^i changes the slope of the corresponding SHMR, whereas the f_*^i factors re-scale them up and down. Unlike at lower redshifts (see e.g. Behroozi, Wechsler & Conroy 2013; Mason et al. 2015; Tacchella et al. 2018; Wechsler & Tinker 2018; Yung et al. 2019; Rudakovskyi et al. 2021; Sabti, Muñoz & Blas 2021a,b; Sabti et al. 2021c), for the EoR/CD we are only interested in very low mass haloes ($M_{\rm h} \lesssim 10^{11}\,{\rm M}_\odot$), as those dominate the photon budget compared to the brighter galaxies, which are rare at the redshifts of interest. Therefore, we can ignore the turnover in the SHMR at $M_{\rm h} \gtrsim 10^{11-12}\,{\rm M}_\odot$ commonly attributed to AGN feedback (Qin et al. 2017), and focus on the fainter end of the ACGs that is well characterized by a single power law. Despite their relatively low $f_*^{\rm (III)}$, MCGs are abundant enough to dominate

[6] https://github.com/21cmfast/21CMMC
[7] https://github.com/charlottenosam/21cmfish

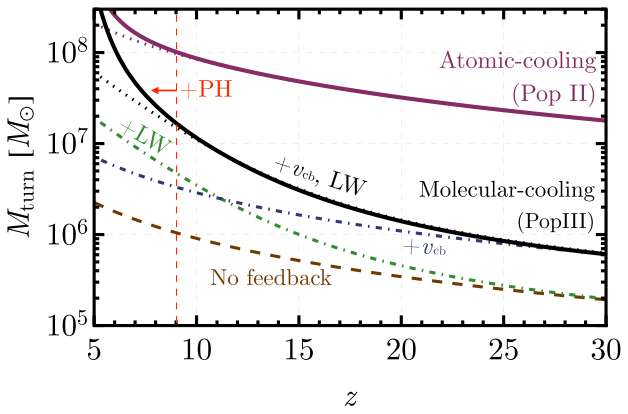

Figure 5. We show different turnover halo mass scales, which enter the SFRDs of Pop II stars in equation (1) and Pop III stars in equation (7). Haloes above the purple line can efficiently cool gas through atomic-line transitions, and we assume they host **ACGs** forming Pop II stars. The dotted purple line is the prediction from $T_{\rm vir} = 10^4$ K, whereas the solid line is the simulation result that includes photoheating (PH) feedback (which is efficient during reionization, to the left of the red line). The dashed brown line represents the theoretical limit above which haloes hosting **MCGs** can form Pop III stars (through molecular cooling) in the absence of feedback. To illustrate the strength of different sources of feedback, we include them one at a time. First, in green we add only LW, and in blue only the streaming velocities ($v_{\rm cb}$). The relative velocities have a bigger impact at high z, whereas LW feedback dominates at later times. We show their product as the black-dotted line, which represents their total feedback from equation (11). The solid black line is the result from the simulation, which again rises sharply during reionization due to photoheating feedback.

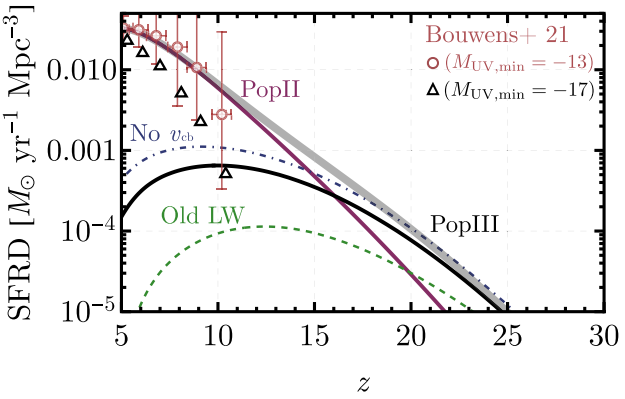

Figure 6. Star formation rate density (SFRD) as a function of z in an average-density region of the universe. The purple and black lines show our prediction for Pop II and Pop III stars hosted in ACGs and MCGs, respectively, and the grey thick line is their sum. The green-dashed line shows the result for Pop III stars if the Machacek et al. (2001) LW feedback prescription was utilized (given the same LW flux), whereas the blue dash–dotted line represents the Pop III result in the absence of relative velocities. The red data-points are the result of extrapolating the Bouwens et al. (2021) UVLFs to $M_{\rm UV,\,min} = -13$, corresponding to $M_{\rm h} \approx 10\,M_{\rm atom}$ (or $M_{\rm h} = 10^{9-10}\,{\rm M}_\odot$) in our model. We also show, as black triangles, the result when only integrating down to $M_{\rm UV,\,min} = -17$, where we have displaced each triangle by $\Delta z = +0.3$ for better visualization (as well as the lowest-z circle for the same reason).

the SFRD at early times ($z \gtrsim 15$), as we quantify below. In our model, MCGs only form stars for a narrow band of halo masses, which varies with z depending on the dominant feedback process. As a consequence of this narrow mass range, the main parameter that controls Pop III star formation in MCGs is $f_*^{\rm (III)}$, rather than the power-law index $\alpha_*^{\rm (III)}$.

At later times ($z = 7$), feedback severely suppresses MCG star formation. Furthermore, the evolution of the HMF means that their relative abundance (compared to ACGs) decreases. As a result of these two effects, the contribution of MCGs to cosmic radiation fields becomes subdominant by $z \sim 7$ in our fiducial model.

In order to understand how feedback evolves over time, we show the different characteristic mass scales in Fig. 5. Going from lowest to highest, we first show the mass for molecular cooling of gas in the absence of feedback, $M_0(z)$ in equation (11), which grows simply as $(1 + z)^{-3/2}$. We then include the impact of relative velocities (through $f_{v_{\rm cb}}$), and LW feedback (through $f_{\rm LW}$, with the J_{21} flux self-consistently and inhomogeneously computed in our simulation box) individually, as well as jointly.

The impact of $v_{\rm cb}$ is notable at high redshifts, increasing the turnover mass by nearly an order of magnitude, to $M_{\rm turn}^{\rm (III)} \approx 10^6\,{\rm M}_\odot$ at $z = 25$. At lower redshifts ($z \lesssim 12$ for our fiducial parameters), LW radiation dominates over $v_{\rm cb}$ in setting the MCGs turnover mass. At even later times (below $z \sim 8$), photoheating feedback from reionization steeply increases $M_{\rm turn}^{\rm (III)}$, so by the end of our simulations at $z = 5$ there is essentially no star formation in MCGs. We remind the reader that in our model Pop II stars form above the atomic-cooling threshold, also shown in Fig. 5, and those are also affected by photoheating feedback.

Given our fiducial choices, we can compute the SFRD for both Pop II and Pop III on a representative (i.e. average-density) patch of the universe (Madau et al. 1996). We do so in Fig. 6, where we show the individual Pop II and Pop III contributions, as well as their sum. As is clear from this figure, Pop III star formation in MCGs dominates over ACGs at higher redshifts, and for our fiducial parameters this transition takes place at $z \approx 15$. We also show two alternative scenarios of Pop III star formation to illustrate the impact of feedback. In one, we turn-off the relative-velocity ($v_{\rm cb}$) effect, and as a result we would overestimate the SFRD of Pop III stars by 50 per cent. In the other, we use the previous feedback formula from Machacek et al. (2001, corresponding to $A_{\rm LW} = 22$ in equation 13), which did not include self-shielding. In that case the SFRD is reduced by roughly an order of magnitude, with the discrepancy increasing at lower z, where J_{21} is larger (though we note that we use the same J_{21} flux as in the fiducial simulation).

Additionally, we compare our predicted SFRDs with data, obtained by extrapolating the recent measurements from Bouwens et al. (2021). We convert our SFRD to UV luminosities using a constant $\kappa = 1.15 \times 10^{-28}\,{\rm M}_\odot$ s yr^{-1} erg^{-1} (Sun & Furlanetto 2016; Oesch et al. 2018), and extrapolate the Schechter fit from Bouwens et al. (2021, with errors inherited from the uncertainty in the Schechter parameters) to a minimum UV magnitude $M_{\rm UV,\,min} = -13$ (Park et al. 2019), which corresponds to haloes with $M_{\rm h} = 10^{9-10}\,{\rm M}_\odot$ for the redshifts of interest. As expected, ACGs fit all the current ($z \lesssim 10$) data well on their own, as observations cannot reach the fainter MCGs (see for instance Sun et al. 2021 for a SPHEREx forecast).

2.4 Cosmic radiation fields

Using the (inhomogeous) ACG and MCG SFRDs from equations (1) and (7), we compute the corresponding cosmic radiation fields that are relevant for the thermal and ionization evolution of the IGM: soft UV (LW and Lyman series), ionizing and X-ray. `21cmFAST` calculates the radiation field incident on each simulation cell through

a combination of excursion-set photon-counting (for ionizing photons) and light-cone integration (for soft UV and X-rays), accounting also for IGM attenuation/absorption. These procedures are described in detail in, e.g. Mesinger et al. (2011), Mesinger, Ferrara & Spiegel (2013), Sobacchi & Mesinger (2014), and we encourage the interested reader to consult these works for further details. Here, we only summarize the free parameters that are the most relevant for our analysis.

We assume the emissivity for all of the above radiation fields scales with the SFR (equations 1 and 7). To calculate UV emission, we take Pop II/Pop III SEDs from Barkana & Loeb (2005), normalized to have $N^{(i)}_{\gamma/b} = 5000$ and 44 000 ionizing photons per stellar baryon for Pop II and III, respectively. We assume only a fraction $f_{\rm esc}$ of ionizing photons that are produced manage to escape the host galaxy and ionize the IGM. We take a power-law relation for the typical $f_{\rm esc}$ as a function of halo mass (Park et al. 2019):

$$f^{(i)}_{\rm esc} = f^{(i)}_{{\rm esc},m_i} \left(\frac{M_{\rm h}}{M_i}\right)^{\alpha^{(i)}_{\rm esc}} \tag{18}$$

for both stellar populations ($i = \{{\rm II}, {\rm III}\}$), with $M_i = \{10^{10}, 10^7\}$ $M_\odot$ and $m_i = \log_{10}(M_i)$ as before.[8] We choose fiducial parameters in broad accordance with the best fits from the latest observations in Qin et al. (2021b), setting

$$\log_{10} f^{({\rm II})}_{{\rm esc},10} = \log_{10} f^{({\rm III})}_{{\rm esc},7} = -1.35,$$

so the escape fractions from MCGs and ACGs are comparable at their pivot points. We have lowered the ACG escape fraction normalization ($f^{({\rm II})}_{{\rm esc},10}$) by -0.15 with respect to Qin et al. (2021b), in order to allow for an increased (though overall small) MCG contribution to reionization. We assume the same scaling with mass

$$\alpha^{({\rm II})}_{\rm esc} = \alpha^{({\rm III})}_{\rm esc} = -0.3$$

for both populations, as these agree with Lyman α forest + CMB data (Qin et al. 2021b). Under these assumptions, we find that ACG-hosted Pop II stars dominate the ionizing photon budget at $z \leq 15$. This is to be expected, as MCGs are subdominant at lower z, and we agnostically set a (relatively) low value of $f^{({\rm III})}_{\rm esc}$ for Pop III stars.

To calculate X-ray emission we assume a power-law SED with a spectral energy index, α_X, and a low-energy cutoff E_0. X-ray photons with energies below E_0 are absorbed within the host galaxies and do not contribute to ionizing and heating the IGM. This was shown to be an excellent characterization of the X-ray SED from either the hot interstellar medium (ISM) or high-mass X-ray binaries (HMXBs), when emerging from simulated, metal-poor, high-redshift galaxies (Fragos et al. 2013; Pacucci et al. 2014; Das et al. 2017). Both α_X and E_0 control the hardness of the emerging X-ray spectrum, and thus the patchiness of IGM heating. Here, we fix $\alpha_X = 1$, and vary E_0. For our fiducial value, we choose $E_0 = 0.5$ keV, based on the ISM simulations of Das et al. (2017), though we also explore a more optimistic model with a softer SED. The normalization of the X-ray SED is determined by the soft-band (with energies less than 2 keV)[9] X-ray luminosity to SFR parameter, $L_{X,<2{\rm keV}}/{\rm SFR}$. Consistent with simulations of HMXBs in metal-poor environments (Fragos et al. 2013), here we take $\log_{10}(L_{X,<2{\rm keV}}/{\rm SFR}) \approx 40.5$ erg s^{-1} per unit SFR ($M_\odot$ yr^{-1}) for both ACGs and MCGs. Such high values are further supported by recent 21-cm power spectrum upper limits at $z = 8$ from HERA The HERA Collaboration (2022).

[8]While there is no consensus on how the ionizing escape fraction depends on galaxy properties, simulations suggest that a generic power law captures the mass behaviour of the population-averaged $f_{\rm esc}$ (e.g. Paardekooper, Khochfar & Dalla Vecchia 2015; Kimm et al. 2017; Lewis et al. 2020).

[9]Only the soft-band X-ray emission efficiently heats the IGM, as X-rays with $E \gtrsim 1.5$–2 keV have mean free paths longer than the size of the universe at the redshifts of interest.

3 OBSERVABLES DURING THE CD AND EOR

We now use the models for ACGs and MCGs outlined above to predict the evolution of the thermal and ionization state of the IGM at high redshifts. We focus on the contribution of Pop III star-forming MCGs, as their corresponding feedback is the main improvement of this work.

We use two sets of galaxy parameters, *Fiducial (EOS)* and *Optimistic (OPT)*, summarized in Table 1. The fiducial (EOS) uses the same ACG parameters as in Qin et al. (2021b), where such a model was shown to reproduce EoR observables (at redshifts $z \lesssim 10$ when the MCG contribution is negligible). However, we do lower the escape fraction of ACGs slightly ($\Delta \log f^{({\rm II})}_{{\rm esc},10} = -0.15$), so as to allow for a modest contribution of MCGs to the high-redshift tail of the EoR (as could be slightly preferred by the CMB EE PS at $l \sim$ 20–30; e.g. Qin et al. 2020b; Ahn & Shapiro 2021; Wu et al. 2021).

Our Optimistic (OPT) parameter set was chosen in order to enhance the relative contribution of MCGs to the SFRD. Although the actual parameter values are fairly arbitrary (given the lack of MCG constraints), we tuned the OPT model to reproduce the timing of the putative EDGES global 21-cm detection at $z \sim 17$ (Bowman et al. 2018). This is mainly done by increasing the SFRD of minihaloes (through $f^{({\rm III})}_{*,7}$) as well as the softness of the X-ray SED emerging from galaxies (through E_0).

In this section, we introduce the main high-redshift observables using our Fiducial (EOS) model. We will show the impact of Pop III stars and present the 2021 installment of the Evolution Of 21-cm Structure (EOS) project, whose goal is to show the state of knowledge of the astrophysics of cosmic dawn and reionization. Later in Sections 4 and 5, when we study parameter variations and VAOs, we will mainly focus on the optimistic (OPT) model.

3.1 UV luminosity functions

The first observable we show are UVLFs. Although limited to comparably brighter galaxies during the EoR/CD, UVLFs detected with the *HST* provided invaluable insights into galaxy formation and evolution at $z \leq 10$.

We follow Park et al. (2019), where the 1500 Å luminosity is obtained from the SFR with a conversion factor of $\kappa = 1.15 \times 10^{-28}$ $M_\odot$ s yr^{-1} erg^{-1} (Sun & Furlanetto 2016; Oesch et al. 2018), and for simplicity we take κ to be the same for both Pop II and Pop III populations. Detailed population-synthesis models suggest that there could be a factor of $\sim$2 variation in this conversion, based on the IMF, metalicity, and star formation history (e.g. Wilkins, Lovell & Stanway 2019).

We show the predicted UVLFs for our fiducial (EOS2021) parameters in Fig. 7, which matches very well the observational data from Bouwens et al. (2015, 2016) and Oesch et al. (2018). This is by construction, as our parameters are motivated by the maximum a posteriori (MAP) model from Qin et al. (2021b), which included UVLFs (in addition to other EoR observables) in the likelihood.

We note that the atomic-cooling threshold $M_{\rm atom} = 2 \times 10^8$ $M_\odot$ at $z = 6$ corresponds to $M_{\rm UV} \approx -9$ in our model, making it difficult to directly observe the even fainter MCGs. This is clear in our Fig. 7, where MCGs only dominate at fainter magnitudes, beyond the reach of even *JWST*. We note that previous work (e.g. O'Shea et al. 2015;

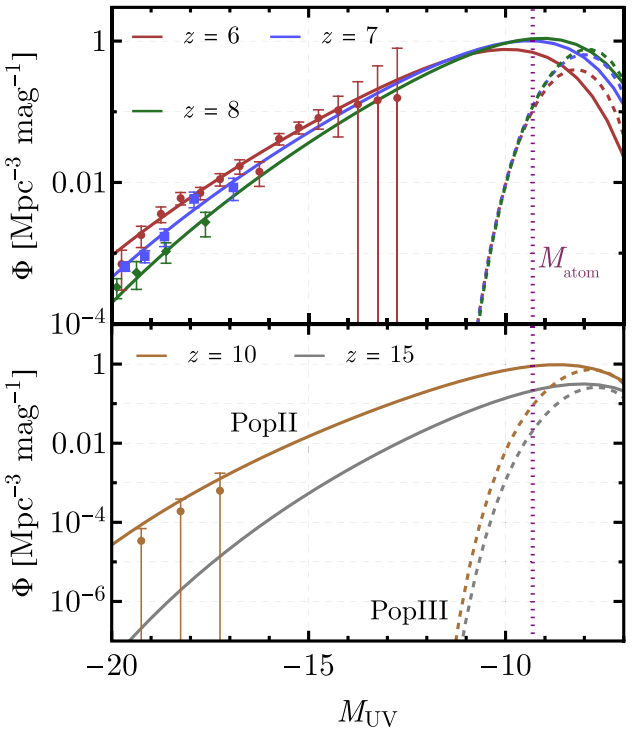

Figure 7. UVLFs at five redshifts for our EOS fiducial parameters, where the solid and dashed lines represent the ACG and MCG contribution, respectively. The data points are from Bouwens et al. (2015, 2016) and Oesch et al. (2018), where only galaxies with $M_{\rm UV} \geq -20$ are shown as these dominate the cosmic radiation backgrounds at the high redshifts of interest. The top panel shows $z = 6$–8, where the data covers a broader magnitude range, whereas the bottom panel focuses on earlier epochs, where only some data are available at $z = 10$. The vertical dotted line shows the magnitude expected of a halo with $M_{\rm h} = M_{\rm atom}$ at $z = 6$, illustrating that in our model MCGs are far too faint to be directly detectable through the UVLF. Nevertheless, these data allow us to constrain the SHMR of ACGs, and thus isolate the contribution of MCGs to cosmic radiation fields using 21-cm observations.

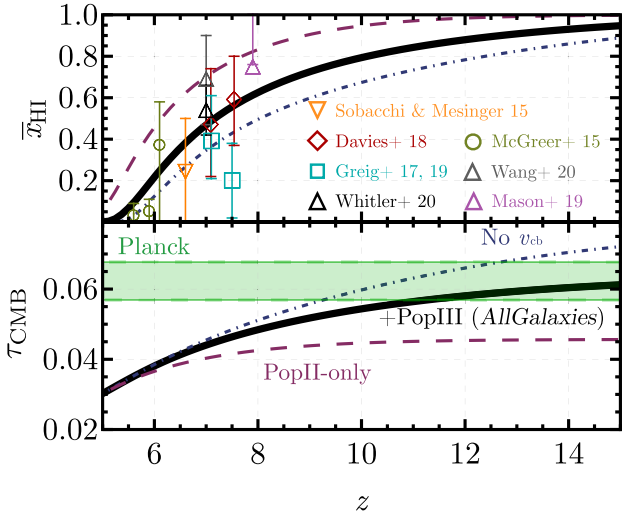

Figure 8. Neutral-hydrogen fraction (**top**) and optical depth to reionization (**bottom**) as a function of redshift z. The black thick line shows our fiducial (EOS2021) model, including both Pop II and Pop III contributions, whereas the purple line is the result from a Pop II-only simulation. The blue dot–dashed curve shows the result of a simulation with no $v_{\rm cb}$ feedback, which produces larger stellar formation at earlier times, and would be above the 1σ measurement of $\tau_{\rm CMB}$ with *Planck* data (de Belsunce et al. 2021), shown as the green band.

Xu et al. 2016b; Qin et al. 2021a), found a turnover for MCGs at even fainter magnitudes ($M_{\rm UV} \gtrsim -7 - -6$). This difference is due to our feedback prescriptions, including relative velocities that dominate at early times (c.f. Fig. 5). As a consequence, the UVLF for MCGs is always below (or comparable to) that of ACGs in Fig. 7. We stress that even though we are unlikely to observe such ultrafaint magnitudes, UVLFs provide an invaluable data set by allowing us to anchor the SHMR scaling relations at the brighter end that is well probed by observations ($-20 \lesssim M_{\rm UV} \lesssim -15$).

Through the rest of this section we will study how the inclusion of Pop III-hosting MCGs – and the $v_{\rm cb}$ feedback on them – affects reionization and the 21-cm signal. We will do so by comparing our best-guess EOS fiducial simulation to one without MCGs, as well as one with both ACGs and MCGs but no relative velocities (similar to Qin et al. (2020a) though with an updated LW feedback prescription).

3.2 EoR history

We show the evolution of the EoR from our Fiducial model (EOS2021) in Fig. 8. We plot both $\bar{x}_{\rm HI}$ and the optical depth $\tau_{\rm CMB}$ of the CMB due to reionization, as a function of z. Given our fiducial parameters, MCGs only make a small contribution to cosmic reionization, and chiefly at high z. The overall evolution of $x_{\rm H\,I}$ agrees broadly with current measurements from McGreer, Mesinger & D'Odorico (2015), Greig et al. (2017, 2019), Mason et al. (2019a), Whitler et al. (2020), Wang et al. (2020), and *Planck* 2018 temperature and polarization (reanalysed in de Belsunce et al. 2021). This is mostly by design, as our ACG (Pop II) parameters were chosen to be consistent with Qin et al. (2021b), who used various EoR observables to constrain the EoR history. In particular, the final overlap stages of reionization are constrained by observations of the Lyman α opacity fluctuations. Qin et al. (2021b) found that the latest forest spectra require a late end to reionization at $z \sim 5.5$ (see also e.g. Kulkarni et al. 2019; Keating et al. 2020; Nasir & D'Aloisio 2020; Choudhury et al. 2021).

The contribution of MCGs would however be largest during the earliest stages of the EoR. In our fiducial model Pop III-hosting MCGs drive a modest increase of the CMB optical depth: $\Delta\tau_{\rm CMB} \approx 0.015$ (though the precise value is sensitive to our fairly arbitrarily chosen MCG parameters). As seen from the figure, this contribution is mostly sourced at $z \sim$ 8–12, with the very high-z tail only contributing $\tau(z = 15\text{–}30) = 2 \times 10^{-3}$, well below the limit of 0.02 from *Planck* 2018 (Millea & Bouchet 2018; Heinrich & Hu 2021). While further data from CMB experiments will more precisely pinpoint $\tau_{\rm CMB}$ (Abazajian et al. 2016; Ade et al. 2019), it will be difficult to isolate the high-z contribution that could be caused by MCGs (Wu et al. 2021). We note that ignoring $v_{\rm cb}$ feedback roughly doubles the contribution of MCGs to reionization, for our fiducial parameter choices.

In Fig. 9, we compare our fiducial, EOS2021 EoR history to that of the EOS2016 release (Mesinger et al. 2016). The 2016 release was comprised of two models, *FaintGalaxies* and *BrightGalaxies*, both of which only included Pop II-hosting ACGs but assumed different turnover mass scales for SNe feedback. In this work, we assume SNe feedback does not induce a turnover, and include also Pop III-hosting MCGs with the associated LW and $v_{\rm bc}$ feedback followed self-consistently. To make this distinction explicit, we denote our EOS2021 model as *AllGalaxies* in the figure.

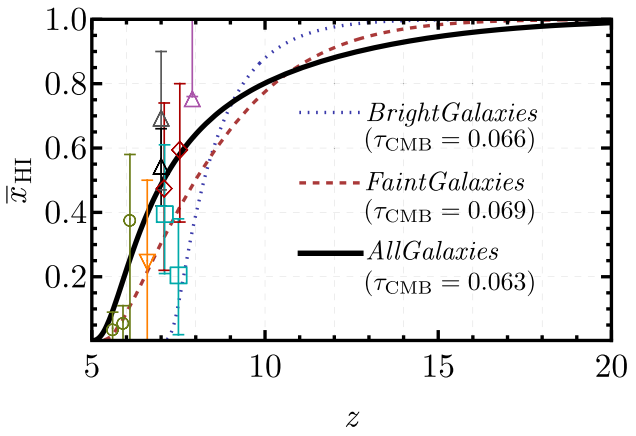

Figure 9. Global neutral-hydrogen fraction for our new 2021 EOS (*AllGalaxies*) simulation in black, compared against the 2016 EOS simulations of Mesinger et al. (2016, *Bright* and *FaintGalaxies* in blue and red, respectively). The $\bar{x}_{\rm HI}$ datapoints are the same as in Fig. 8, and we write the integrated optical depth $\tau_{\rm CMB}$ for each simulation.

All EOS releases are 'tuned' to reproduce the current state of knowledge. In 2016, our estimate of τ_e and forest data suggested an earlier middle/end of reionization, as is reflected in this comparison plot. The shapes of the EoR histories are also notably different. By including MCGs, *AllGalaxies* (EOS2021) produce a more extended tail to higher redshifts, with percent level ionization up to $z \sim 20$. Despite this earlier start, the ACG-driven mid and late stages of reionization occur *more rapidly* in *AllGalaxies* than in *FaintGalaxies*. This is because both EOS2016 models assumed a constant mass-to-light ratio ($\alpha_*^{\rm (II)} = 0$). This assumption, albeit common, is inconsistent with the latest UVLF observations and overestimates star formation in small galaxies, thus resulting in a slower evolution of the SFRD and associated cosmic epochs (see also Mirocha et al. 2017; Park et al. 2019). This figure highlights the importance of using the latest observations to guide our models of the early universe.

3.3 The 21-cm line during the cosmic dawn

The biggest impact from MCGs will be to the cosmic-dawn epoch, which we mainly observe through the 21-cm line of neutral hydrogen. We now explore this observable.

We first show our definitions, and refer the reader to Furlanetto, Oh & Briggs (2006) and Pritchard & Loeb (2012) for detailed reviews of the physics of the 21-cm line. We use the full expression for the 21-cm brightness temperature (Barkana & Loeb 2001)

$$T_{21} = \frac{T_S - T_{\rm CMB}}{1+z}\left(1 - e^{-\tau_{21}}\right), \tag{19}$$

where $T_{\rm CMB}$ is the temperature of the CMB (which acts as the radio back light), T_S is the spin temperature of the IGM, and

$$\tau_{21} = (1+\delta) x_{\rm H\,I} \frac{T_0}{T_S} \frac{H(z)}{\partial_r v_r}(1+z), \tag{20}$$

where $\partial_r v_r$ is the line-of-sight gradient of the velocity. We have defined a normalization factor

$$T_0 = 34\,{\rm mK}\left(\frac{1+z}{16}\right)^{1/2} \times \left(\frac{\Omega_{\rm b}\,h^2}{0.022}\right)\left(\frac{\Omega_{\rm m}\,h^2}{0.14}\right)^{-1/2} \tag{21}$$

anchored at our *Planck* 2018 cosmology.

The spin temperature of hydrogen, which determines whether 21-cm photons are absorbed from the CMB (if $T_S < T_{\rm CMB}$) or emitted (for $T_S > T_{\rm CMB}$), is set by competing couplings to the CMB and to the gas kinetic temperature T_K, and can be found through

$$T_S^{-1} = \frac{T_{\rm CMB}^{-1} + x_\alpha T_\alpha^{-1} + x_c T_K^{-1}}{1 + x_\alpha + x_c}, \tag{22}$$

where T_α is the colour temperature (which is closely related to T_K, Hirata 2006), and x_i are the couplings to T_K due to Lyman α photons (x_α) through the Wouthuysen–Field effect (Wouthuysen 1952; Field 1959) and through collisions (x_c, which are only relevant in the IGM at $z \gtrsim 30$, Loeb & Zaldarriaga 2004).

There are two main avenues for measuring the 21-cm signal. The first is by through its monopole against the CMB, usually termed the *global signal* (GS hereafter). The second is through the fluctuations of the signal, commonly simplified into the Fourier-space two-point function or *power spectrum* (PS hereafter). We now explore each in turn.

3.3.1 Global Signal

The 21-cm GS (denoted by $\overline{T}_{21}$) is currently targeted by experiments such as EDGES (Bowman et al. 2018), LEDA (Price et al. 2018), SARAS (Singh et al. 2018), Sci-Hi (Voytek et al. 2014), and Prizm (Philip et al. 2019). We note however that the lack of angular information makes the GS especially difficult to disentangle from foregrounds, which can be several orders of magnitude stronger than the cosmic signal.

We show our predictions for the 21-cm GS in Fig. 10. The 21-cm signal is characterized three well-known eras at high z. First, there is the epoch of coupling (EoC, $z \sim$ 15–25 for our EOS parameters), where the GS $\overline{T}_{21}$ becomes more negative due to the Wouthuysen–Field (WF) coupling sourced by the Lyman-series photons from the first galaxies (Wouthuysen 1952; Field 1959). Then, there is the epoch of X-ray heating (EoH), where X-rays emitted by galaxies heat up the IGM, slowly increasing $\overline{T}_{21}$ until it is above zero. Finally, during the EoR $\overline{T}_{21}$ is driven towards zero following $\overline{x}_{\rm HI}$.

The difference between models with Pop II only and with Pop III stars is dramatic, as shown in the top panel of Fig. 10. This is to be expected, as the high-z SFRD is dominated by the smaller (and thus more abundant) MCGs. Ignoring Pop III-dominated MCGs delays the minimum in the GS from $z \approx 15$ to $z \approx 12.5$, and results in a more rapid evolution of all epochs (EoC, EoH, and EoR). The top panel of Fig. 10 also shows that neglecting $v_{\rm cb}$ feedback shifts the EoC and EoH earlier by $\Delta z \approx +2$, which highlights the importance of this effect during the cosmic dawn.

We also compare the GS of the fiducial EOS2021 simulation against the previous two models of EOS2016. The most striking distinction between these three simulations is that the depth for the new EOS2021 (*AllGalaxies*) model is a factor of 2 shallower than for both EOS 2016 simulations, only reaching values of $\overline{T}_{21} \approx -70$ mK. As already discussed, the emissivity in the 2016 simulations did not follow the SHMR implied by UVLFs but was instead proportional to the collapsed-fraction (equivalent to a constant f_* in Fig. 4). As a consequence, the SFRD in those models evolved more rapidly, producing more distinct EoC and EoH epochs, whereas in the realistic *AllGalaxies* model these overlap (see also Mirocha et al. 2017; Park et al. 2019; Qin et al. 2020a).

Such a shallower absorption trough also has implications for exotic cosmic explanations of the recent EDGES detection (Bowman et al. 2018); though we caution that a cosmological interpretation of the detected signal remains very controversial (Hills et al. 2018;

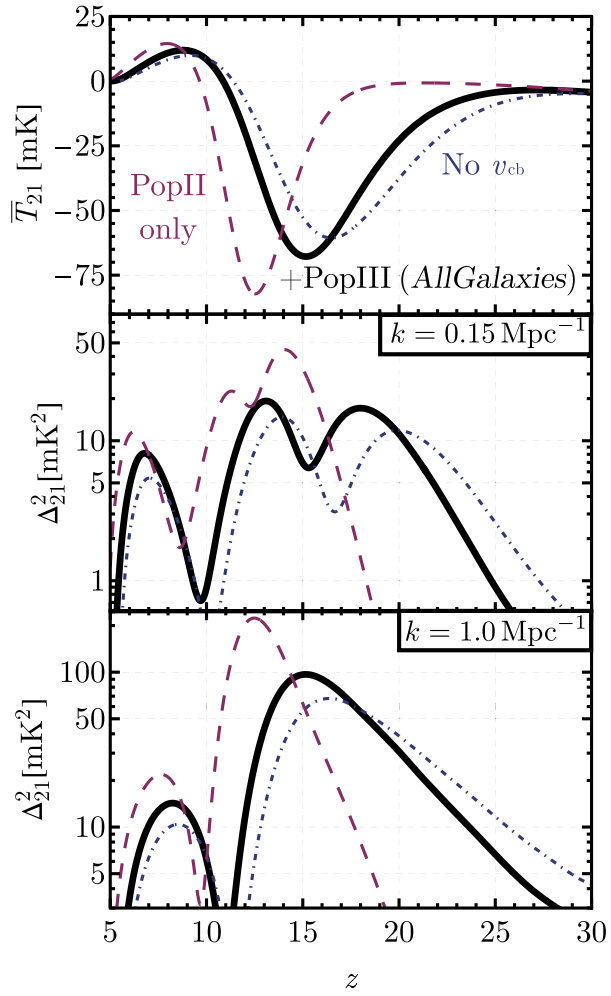

Figure 10. Evolution of the 21-cm signal, as a function of redshift z, across the entire CD and the EoR, for different models. The **top** panel shows the 21-cm global signal (GS), the whereas the **middle** and **bottom** panels show the 21-cm power spectrum (PS) at two different wavenumbers: $k = 0.15$ and $1.0\,\mathrm{Mpc}^{-1}$, respectively. As before, the black line shows our fiducial EOS model with Pop II and Pop III stars with all feedback considered, whereas the blue dash–dotted line does not consider feedback due to the streaming velocities v_{cb}, and the purple dashed line only has Pop II stars. The Pop II-only case shows a markedly delayed 21-cm evolution, as the GS in the top panel does not turn into absorption until $z \sim 15$, whereas the case with Pop III stars begins its descent around $z \sim 22$, reaching a minimum at $z \approx 15$. The no-v_{cb} case has much faster evolution, especially at higher z, due to the absence of v_{cb}-induced feedback on the first galaxies. The 21-cm PS at large scales ($k = 0.15\,\mathrm{Mpc}^{-1}$) and small scales ($k = 1.0\,\mathrm{Mpc}^{-1}$) follow a similar pattern, though the large-scale one close to vanishes at the minima and maxima of the GS (Muñoz & Cyr-Racine 2021).

Sims & Pober 2020). The lowest point of our trough ($\overline{T}_{21} \approx -70$ mK) is roughly a factor of 7 shallower than claimed by EDGES ($\overline{T}_{21} \approx -500$ mK), requiring either stronger dark matter electric charges (e.g. Barkana 2018; Muñoz & Loeb 2018), or a brighter extra radio background (e.g. Ewall-Wice et al. 2018; Pospelov et al. 2018) than previously assumed. However in terms of timing, our fiducial EOS model (with Pop III stars) peaks at $z \sim 15$, only slightly later than the timing of the first claimed EDGES detection (at $z \approx 17$). We will study a different set (OPT) of MCG parameters in Sections 4 and 5, which give rise to an absorption trough at an earlier $z \approx 17$.

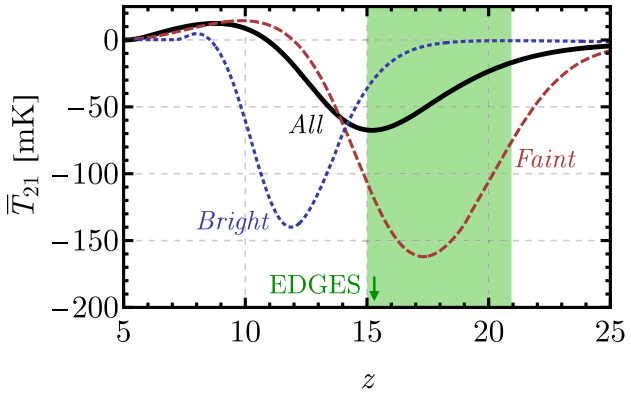

Figure 11. Global 21-cm brightness temperature for the 2016 EOS simulations of *Bright* and *FaintGalaxies* (from Mesinger et al. 2016), in blue and red, respectively, as well as the new *AllGalaxies* simulation presented here, in black. The green region shows the range of the claimed EDGES detection Bowman et al. (2018, though its depth of $\overline{T}_{21} \approx -500$ mK is below the range of this plot).

3.3.2 *Power spectrum*

We now study the 21-cm fluctuations. For simplicity, we will focus on the spherically averaged PS summary statistic, defined through

$$\left\langle \delta T_{21}(\mathbf{k}) \delta T_{21}(\mathbf{k}') \right\rangle = (2\pi)^3 \delta_D(\mathbf{k} + \mathbf{k}') P_{21}(\mathbf{k}), \tag{23}$$

although in practice we will employ the reduced power spectrum $\Delta^2_{21} = k^3 P_{21}(k)/(2\pi^2)$, with units of mK^2, for convenience. Interferometers can measure many 21-cm modes at each z, and thus the PS (and other spatially dependent statistics) can provide more detailed insights into the early universe, compared to the GS (Pritchard & Furlanetto 2007; Parsons et al. 2012; Pober et al. 2013b; Fialkov & Barkana 2014; Cohen, Fialkov & Barkana 2018; Muñoz, Dvorkin & Cyr-Racine 2020; Jones et al. 2021). Experiments such as HERA (DeBoer et al. 2017), LOFAR (van Haarlem et al. 2013), MWA (Tingay et al. 2013), LWA (Eastwood et al. 2019), and the SKA (Koopmans et al. 2015) are aiming to measure the 21-cm PS.

We show the evolution of the 21-cm PS at two different Fourier-space wavenumbers k in Fig. 10 (along with the GS for visual aid). The large-scale ($k = 0.15\,\mathrm{Mpc}^{-1}$) power has three bumps, corresponding to the three eras outlined above, when fluctuations in the Lyman α background, IGM temperature, and ionization fractions dominate the 21-cm PS, respectively. Between these, the negative contribution of the cross power between these fields gives rise to relative troughs in the PS (Pritchard & Furlanetto 2007; Lidz et al. 2008; Mesinger et al. 2013) (and as a result $\Delta^2_{21} \propto \mathrm{d}T_{21}/\mathrm{d}z$ on large scales Muñoz & Cyr-Racine 2021). At smaller scales ($k = 1.0\,\mathrm{Mpc}^{-1}$), however, this cancellation does not take place, and the power is larger overall. The power is larger for the Pop II-only model at both large and small scales, as the smaller-mass MCGs that host Pop III stars are less biased, producing smaller 21-cm fluctuations. The absence of v_{cb} feedback shifts all curves towards earlier times. Moreover, as we will see in Section 5, the v_{cb} fluctuations become imprinted on to the 21-cm PS (Dalal et al. 2010; Visbal et al. 2012; Muñoz 2019a), giving rise to sizable wiggles on the 21-cm power spectrum.

In Fig. 12, we compare the PS from our fiducial EOS2021 model (*AllGalaxies*), to the previous EOS2016 models (*BrightGalaxies* and *FaintGalaxies*). The newer *AllGalaxies* model shows significantly smaller power during the cosmic dawn than both EOS 2016

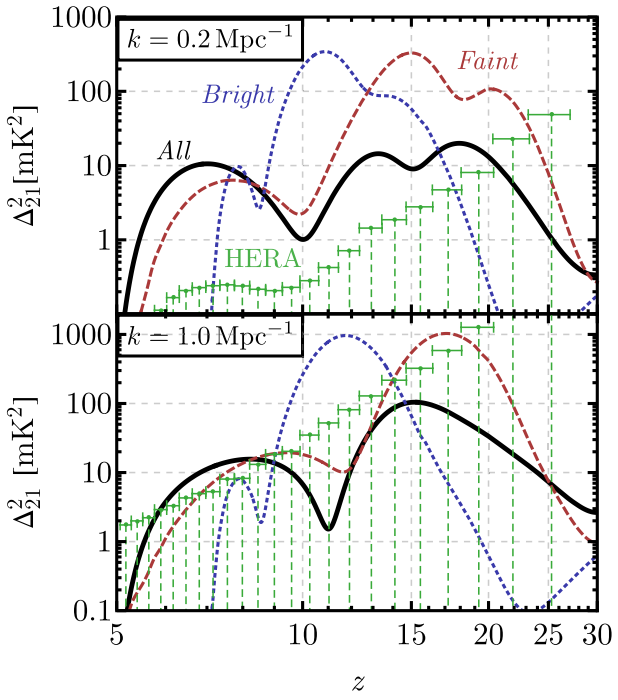

Figure 12. The 21-cm power spectrum at two wavenumbers $k = 0.2$ and 1.0 Mpc^{-1} for all EOS simulations, with the same colour coding as Fig. 11. We additionally show the expected noise from HERA in different z bands (all corresponding to a bandwidth of $B = 8$ MHz), where we assume 180 d of observation, moderate foregrounds, and $\Delta k = 0.1\,\mathrm{Mpc}^{-1}$. We have taken *AllGalaxies* as the fiducial for the cosmic-variance noise, and find a total SNR = 183 added in quadrature over k and z.

predictions. That is because of both the shallower absorption – and slower evolution – of the 21-cm global signal. This reduction reaches an order of magnitude at $z \geq 10$, and will hinder the observation of the 21-cm power spectrum with interferometers.

Nevertheless, our *AllGalaxies* 21-cm power spectrum is still significantly above the thermal noise level forecasted for upcoming interferometers like HERA and SKA. We show in Fig. 12 the expected noise after 1 yr (1080 h) of integration with HERA, calculated with `21cmSense`[10] (Pober et al. 2013a; Pober et al. 2014) under the moderate-foreground assumption with a buffer $a = 0.1\,h\mathrm{Mpc}^{-1}$ above the horizon. We assume a fixed bandwidth of 8 MHz (corresponding to $\Delta z = 0.7$ at $z = 10$), spherical bins of $\Delta k = 0.1\,\mathrm{Mpc}^{-1}$, and a system temperature (DeBoer et al. 2017)

$$T_{\rm sys}(\nu) = 100\,\mathrm{K} + 120\,\mathrm{K} \times \left(\frac{\nu}{150\,\mathrm{MHz}}\right)^{-2.55}. \quad (24)$$

This results in a noise that is below the signal up to $z \approx 20$ at large scales, and comparable to the signal at small scales. At low k, the noise is dominated by cosmic variance, which tracks the amplitude of the PS, whereas for at high k it is largely thermal.

We further quantify the detectability of our EOS 2021 model (*AllGalaxies*), by computing the signal-to-noise ratio (SNR). We calculate this quantity for each wavenumber k and redshift bin z considered, and add them in quadrature. We consider two values for $T_{\rm sys}$, that of equation (24) and a more pessimistic one of

$$T^{\rm pess.}_{\rm sys}(\nu) = 100\,\mathrm{K} + 400\,\mathrm{K} \times \left(\frac{\nu}{150\,\mathrm{MHz}}\right)^{-2.55}, \quad (25)$$

[10] https://github.com/jpober/21cmSense

Table 2. SNR for the two interferometers we consider, under a regular system-noise assumption, given by equation (24), and a pessimistic one, from equation (25). The three epochs cover the ranges of $z \leq 10$ for the EoR, $10 < z < 15$ for the EoH, and $z \geq 15$ for the EoC.

SNR for EOS2021	Total	EoR	EoH	EoC
HERA	186	183	34	9
HERA (pess.)	87	86	8	1
SKA	164	157	41	22
SKA (pess.)	85	84	12	4

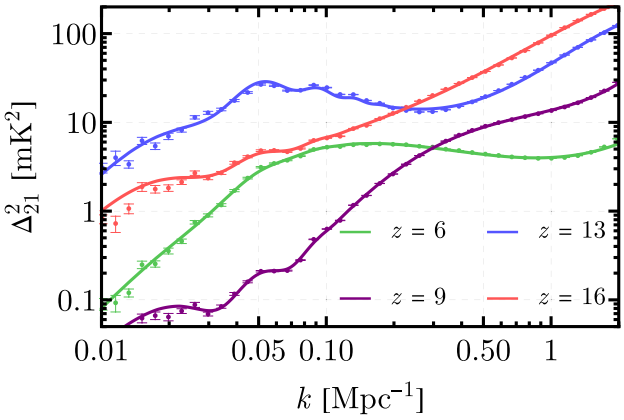

Figure 13. Power spectrum of 21-cm fluctuations as a function of wavenumber k for our *AllGalaxies* (EOS2021) simulation. The four redshifts are chosen to be during the EoC ($z = 16$), halfway through the EoH ($z = 13$), in the transition between the EoH and the EoR ($z = 9$), and finally during the EoR ($z = 6$). The small error bars come from the Poisson noise in our box, which is 1.5 Gpc comoving in size. The lines represent a fit (using $k = 0.02$–$0.5\,\mathrm{Mpc}^{-1}$) to a smooth polynomial added to the wiggles from the VAOs (sourced by the streaming velocities $v_{\rm cb}$), as we will explain in Section 5.

following Dewdney et al. (2016), which results in a noise larger by a factor of ∼3 at the redshifts of interest. We also calculate the SNR for the fiducial SKA-LOW 1 design Dewdney et al. (2016) using a tracked observing strategy. Specifically, we assume a 6 h per-night tracked scan for a total of 1000 h. Table 2 shows the SNRs for the different setups, where using equation (24) we find SNR = 186 for HERA and SNR = 164 for the SKA, both of which would provide detections at high significance. These SNRs would be reduced by a factor of ∼2–3 for the pessimistic $T_{\rm sys}$ from equation (25). Divided into epochs, the SNR is significantly dominated by the EoR, with the EoH contributing a factor of ∼5 less, and the EoC only showing SNR ∼10. Interestingly, for our fiducial 'narrow and deep' SKA survey, the SKA can reach larger SNR at high z where thermal noise dominates, while HERA performs better at lower z where cosmic variance can be dominate the noise. Assuming different SKA observing strategies can shift the balance between cosmic-variance and thermal-noise errors by considering either larger observing volumes or deeper integration times (see e.g Greig, Mesinger & Koopmans 2020a). We will explore in Mason et al. (in preparation) the range of constraints that such a detection would provide for astrophysical and cosmological parameters.

Finally, we show the scale dependence of the 21-cm PS at four redshifts in Fig. 13. These are chosen to illustrate the power spectrum during each of the three epochs of interest (EoR, EoH, and EoC), as well as in the transition between the EoR and EoH. The power is

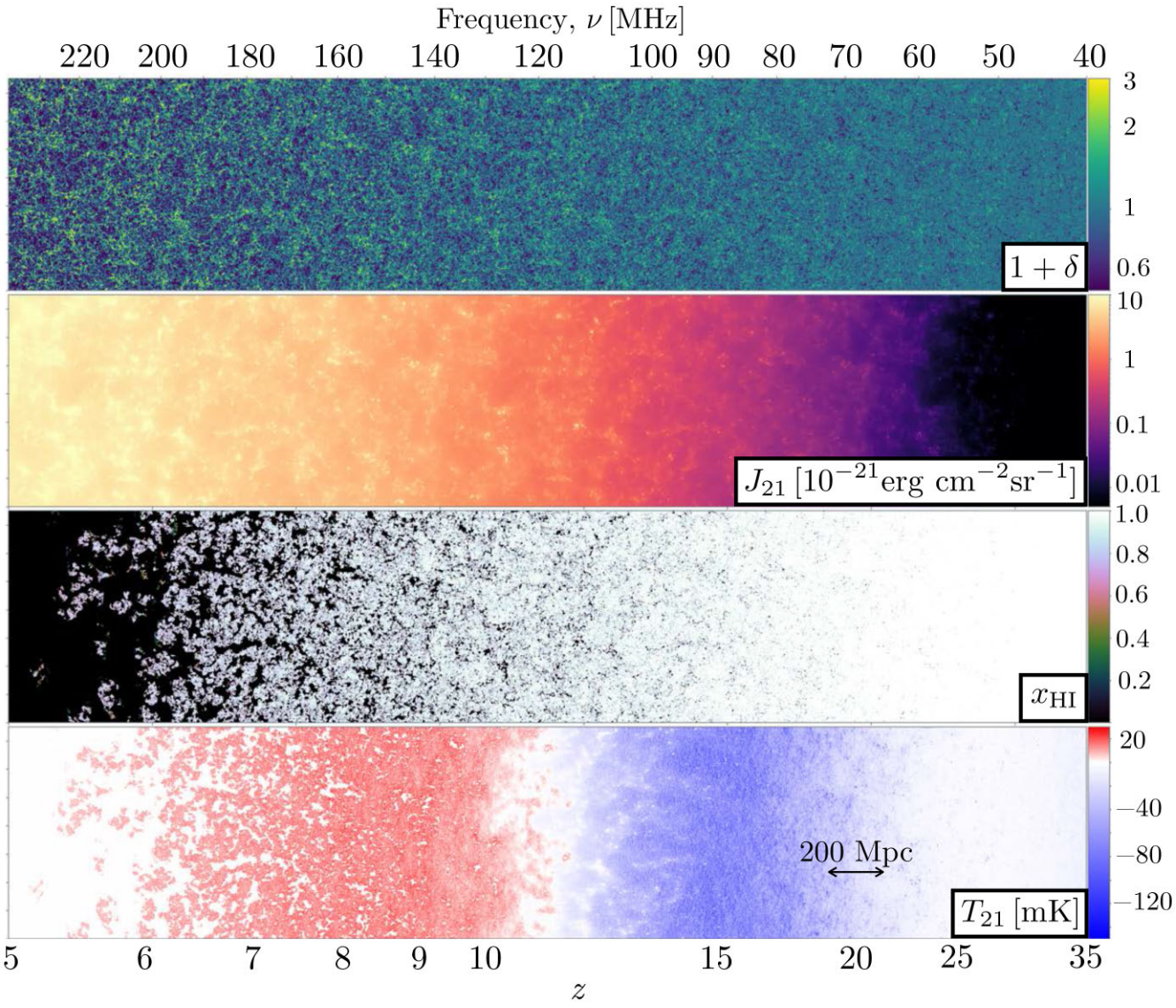

Figure 14. Light-cone from a simulation with the EOS 2021 parameters from Table 1. The slices are 750 Mpc in height (half of the full simulation, for better visualization of small scales), and 1.5 Mpc in depth. The top panel shows the density field, in lognormal scale around unity. The second panel is the LW flux J_{21}, in the customary units of 10^{-21} erg s^{-1} Hz^{-1} cm^{-2} sr^{-1}, which dissociates molecular hydrogen and halts Pop III stellar formation on MCGs. The third panel is the neutral-hydrogen fraction $x_{\rm H\,I}$, which shows the overall evolution of reionization, as well as the large-scale neutral patches at $z \sim 6$ that can explain opacity fluctuations seen in the Lyman α forest. Finally, the bottom panel is the 21-cm signal T_{21} in mK, where the absorption (blue) trough occurs at $z \sim 15$, the transition to emission (red) at $z \sim 10$, and the signal disappears (white) due to reionization by the end of the simulation.

relatively flat with k except in the transition case ($z = 9$), where the large-scale power drops dramatically due to the negative contribution of the cross-terms (Pritchard & Furlanetto 2007; Lidz et al. 2008; Mesinger et al. 2013; Muñoz & Cyr-Racine 2021). Interestingly, at $z = 13$ the power peaks at $k = 0.1\,{\rm Mpc}^{-1}$, where there are wiggles in the 21-cm power spectrum. These are due to the streaming velocities $v_{\rm cb}$, which have acoustic oscillations that become imprinted on to the SFRD (through the feedback described in Section 2), and thus on the 21-cm signal. We will describe these velocity-induced acoustic oscillations (VAOs) in detail in Section 5.

3.4 Visualizations

We end this section with some visualizations of our EOS 2021 simulation. These consist of slices through various light-cones and simulation cubes.

We begin with Fig. 14, which shows 2D slices through cosmic light-cones from our fiducial EOS 2021 simulations. The horizontal axis shows evolution with cosmic time, while the vertical axis corresponds to a fixed comoving length (here taken to be half of the full EOS size in order to more easily identify small-scale features). While we only track a few variables in that figure, we note that `21cmFAST` can output other relevant quantities such as the local recombination rate, the intensity of the UV, X-ray, Lyman α backgrounds, the velocity fields, and kinetic and spin temperatures. We describe each of the panels in turn.

(i) The top panel shows the matter over/underdensities, which grow due to gravity as the universe evolves, forming the cosmic web that we see today.

(ii) The second panel of Fig. 14 shows the LW flux, which dissociates H_2 molecules and thus impedes star formation in MCGs.

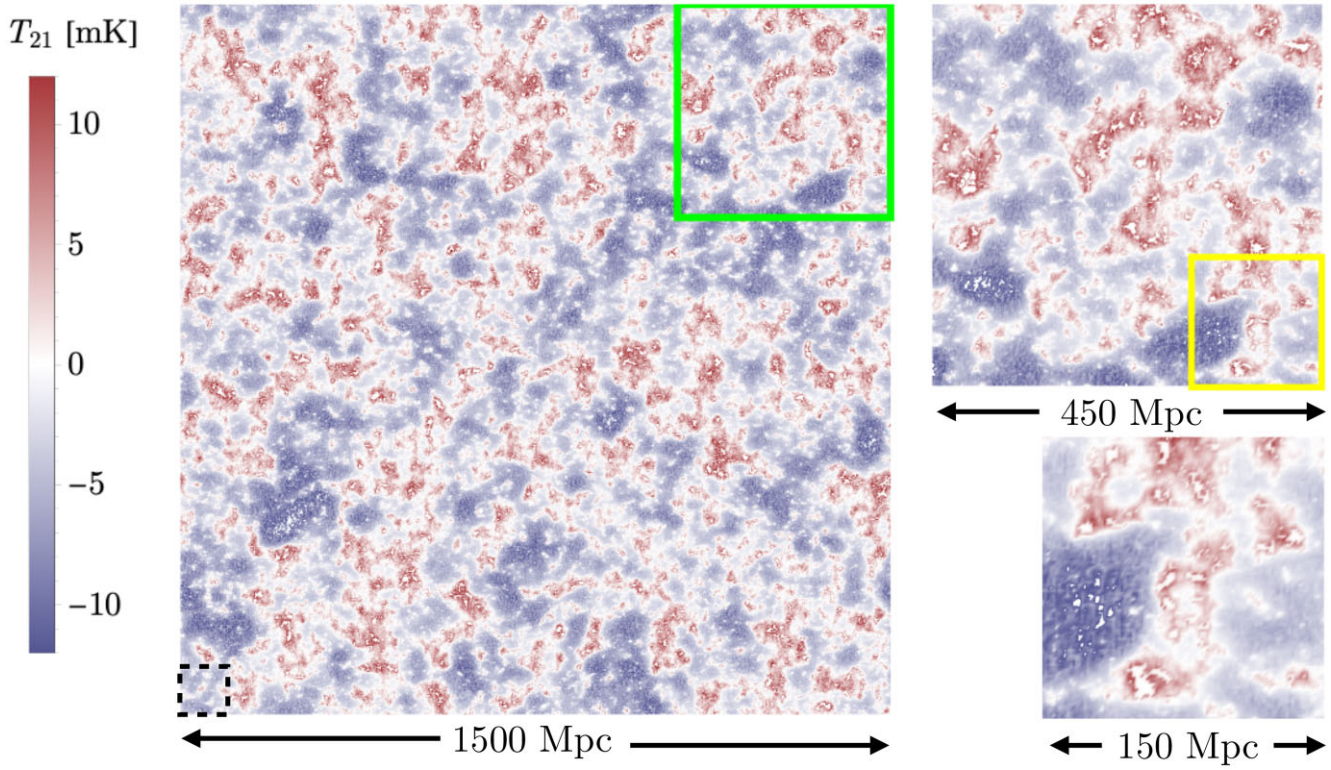

Figure 15. Slice through the 21-cm temperature in our *AllGalaxies* simulation (with the EOS 2021 parameters of Table 1) at $z = 11$. The left-hand panel shows the entire simulation (1.5 Gpc comoving in side), whereas the two right panels represent successive zoom-ins of each of the highlighted regions. For reference, state-of-the-art radiative-transfer hydrodynamical simulations of reionization that resolve ACGs (e.g. Garaldi et al. 2021; Kannan et al. 2021; Smith et al. 2021) can typically cover volumes $\lesssim (100\,\mathrm{Mpc})^3$, shown as the black dashed square on the bottom left. Red and blue corresponds to 21-cm emission and absorption, as in Fig. 14, and all slices are 1.5 Mpc in thickness. At this redshift our model is transitioning from the EoH to the EoR. We see that these two eras overlap, causing the centres of heated regions ($T_{21} > 0$, red), which have the highest densities of galaxies, to show no signal ($T_{21} = 0$, white).

The overall LW flux J_{21} grows rapidly over time (roughly following the SFRD), with notable spatial fluctuations. The LW flux is largest in regions corresponding to the largest matter overdensities, which host the first generations of (highly biased) galaxies. Therefore these anisotropies result in a stronger suppression of Pop III star formation, than would be expected assuming a homogeneous background, and imprint structure in the 21-cm signal.

(iii) The third and fourth panels of Fig. 14 show the evolution of the two quantities most directly observable: the neutral hydrogen fraction $x_{\rm H\,I}$ and the 21-cm brightness temperature T_{21}. The neutral fraction $x_{\rm H\,I}$ is homogeneously close to unity until $z \sim 10$, as chiefly MCGs form at those early times, which are not very efficient at reionizing hydrogen. The EoR takes place during $z = 5$–10, accelerating at later times. This panel reveals large-scale neutral patches at $z \sim 5.5$–6, as required by recent Lyman α data (Becker et al. 2015; Bosman et al. 2018). These last neutral regions trace underdense environments.

(iv) The 21-cm signal T_{21}, in the last panel, shows a dramatic evolution during cosmic dawn, beginning with absorption at $z \sim 15$–20 due to the Wouthuysen–Field effect, followed by a transition to emission at $z \sim 12$ as the IGM is heated by X-rays from the first galaxies, and finishing with a slow decay towards zero as reionization takes place. The late-time ($z \lesssim 10$) behaviour of the 21-cm signal is dominated by the reionization bubbles, as the $x_{\rm H\,I}$ and T_{21} fields are clearly correlated. The early-time ($z \gtrsim 10$) behaviour, however, is related to the UV and X-ray flux from the first galaxies, which depends on the densities δ in a non-linear and non-local way.

In Fig. 15, we show a zoom-in slice through the 21-cm map at $z = 11$. This redshift corresponds roughly to the transition between the EoH and the EoR. It is clear that there is a large overlap between these two eras, as the overdense heated regions (with $T_{21} > 0$, shown in red), are beginning the process of reionization from the inside (producing $T_{21} \to 0$, in white). We note that the underdense regions, exposed to a smaller X-ray flux, are remain colder than the CMB at this redshift ($T_{21} < 0$, in blue).

Fig. 15 also shows the dynamic range of our simulations, which can resolve structure as large as the simulation box (1.5 Gpc) and down to the cell size (1.5 Mpc). A zoom-in animation of the entire cosmic dawn and EoR evolution is provided at this url.

4 LEARNING ABOUT THE FIRST GALAXIES

In the previous sections we have demonstrated that MCGs drive the 21-cm signal from the early cosmic dawn, given our fiducial set of parameters. As a consequence, 21-cm studies are a promising avenue to learn about the properties of the first Pop III stars and their host galaxies. Here, we perform a brief exploratory study of how the 21-cm signal varies as a function of the different MCG stellar and feedback parameters in our model.

Throughout this section, we will vary parameters around a more optimistic set of galaxy properties, labelled *OPT* in Table 1. This set allows for a more significant contribution from MCGs compared to EOS, making it easier to learn about these first galaxies. In particular, we increase the stellar efficiency of MCGs by $\Delta \log_{10} f_{*,10}^{(\rm II)} = -0.75$

(roughly a factor of ≈5), and decrease it for ACGs by $\Delta \log_{10} f_{*,10}^{(\rm II)} = -0.25$, in both cases compensating their $f_{\rm esc}$ to keep a similar EoR evolution. This higher MCG contribution pushes the trough of the 21-cm GS to an earlier $z \sim 17$ (in line with the central redshift claimed by EDGES in Bowman et al. 2018), rather than the $z \sim 15$ of our EOS parameters. We also find that in OPT, Pop III stars dominate the SFRD for $z \gtrsim 10$, thus dictating the evolution of the entirety of cosmic dawn.

We begin by studying the slope of the SHMR, here parametrized with the $\alpha_*^{(\rm III)}$ parameter. The SHMR slope likely holds clues about SNe and other galactic feedback mechanisms. For example, assuming star formation is regulated by SNe-driven outflows with a constant energy coupling efficiency, can result in $\alpha_* \sim 2/3$ (e.g. Wyithe & Loeb 2013). This is remarkably close to the empirically determined value from $z \gtrsim 6$ UVLFs of $\alpha_*^{(\rm II)} \sim 0.5$ (for ACGs hosting Pop II stars).

As discussed previously, ACGs are too faint to allow us to directly measure $\alpha_*^{(\rm III)}$ from UVLFs. Although it is tempting to assume the same SHMR slope for ACGs and MCGs, this could be incorrect due to, e.g. their different IMFs and associated SNe energies. For example, a fixed mass of stars forming in each MCG (e.g. Kulkarni et al. 2019) would result in $\alpha_*^{(\rm III)} < 0$, which would be very different from the $\alpha_*^{(\rm II)} \sim 0.5$ that is empirically determined from $z \gtrsim 6$ UVLFs.

In Fig. 16, we show the impact of varying the power-law index $\alpha_*^{(\rm III)}$ on the 21-cm CD signal (global and power spectrum evolution). We consider $\alpha_*^{(\rm III)}$ in the −0.2–0.5 range. It is clear that the 21-cm signal does not vary dramatically over this range of SHMR slopes. Steeper indices (larger $\alpha_*^{(\rm III)}$) effectively result in steeper SFRD evolutions at very high redshifts. Although initially there are fewer Pop III stars in those models, delaying the 21-cm signal, subsequently the cosmic evolution accelerates.

Interestingly, all models in Fig. 16 agree at $z \approx 15$, when the contribution from ACGs starts being relevant. However, we do see that the J_{21} evolution of some models crosses-over around this redshift (c.f. the green curve). This is due to LW feedback: models that initially have a larger J_{21} are subsequently able to more strongly quench MCG star formation, thus resulting in a weaker J_{21} at $z < 15$.

We now study the impact of the other parameters regulating the UV and X-ray emissivities of MCGs. Specifically, in Fig. 17 we show how the 21-cm GS and PS (at $k = 0.15\,{\rm Mpc}^{-1}$) vary with: (i) $A_{\rm LW}$, the amplitude of LW feedback; (ii) $f_{*,7}^{(\rm III)}$, the normalization of the SHMR; (iii) $f_{\rm esc,7}^{(\rm III)}$, the ionizing escape fraction; and (iv) $L_{X,<2{\rm keV}}^{(\rm III)}/{\rm SFR}$, the X-ray luminosity to SFR relation. Unlike for $\alpha_*^{(\rm III)}$ discussed above, the uncertainty on these parameters is better sampled in log space. Therefore in Fig. 17 we show results when increasing or decreasing each parameter by a factor of three around the *OPT* values from Table 1.

The first panel of Fig. 17 shows that stronger LW feedback (larger $A_{\rm LW}$) translates into a delayed 21-cm GS and PS, especially at high z. The larger impact of other feedback sources, chiefly the relative velocities, makes the signal depend only weakly on $A_{\rm LW}$, though this parameter can still delay the cosmic-dawn milestones by $\Delta z \approx 1$ within the range of values we study.

Changing $f_{\rm esc,7}^{(\rm III)}$ also has a modest impact, as MCGs are generally negligible contributors to the EoR in our models. However, the largest values of the escape fraction shown here do result in an earlier start to the EoR (driven by MCGs), but with a similar end (driven by ACGs).

On the other hand, varying the stellar fraction $f_{*,7}^{(\rm III)}$ (second panel) or $L_{X,<2{\rm keV}}^{(\rm III)}/{\rm SFR}$ (fourth panel) notably changes the signal during the two CD epochs driven by MCGs: the EoH and EoC. Changing the stellar fraction impacts both epochs, as star formation drives all of the cosmic radiation fields in our models. Higher stellar fractions shifts the CD to earlier times, resulting in a higher effective bias of the sources driving each epoch, and thus a higher 21-cm PS on large scales.

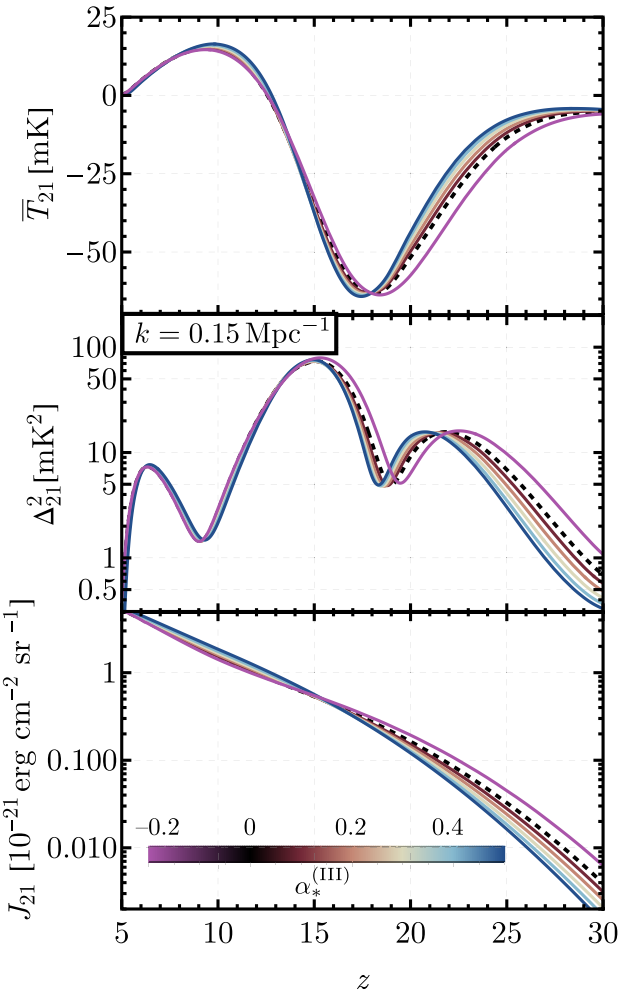

Figure 16. Predictions for the evolution of the 21-cm GS (top), PS (middle), and the LW flux (bottom) across CD and the EoR, when varying the slope of the SHMR of MCGs. We consider a range of power-law indices $\alpha_*^{(\rm III)}$ of the SHMR, as defined in equation (7), from $\alpha_*^{(\rm III)} = 0$ (our fiducial, in black) to 0.5 (red to blue lines), as well as $\alpha_*^{(\rm III)} = -0.2$ (in pink, corresponding to a reversed SHMR). Steeper $\alpha_*^{(\rm III)}$ indices produce less star formation at early times, delaying the onset of cosmic dawn (top two panels). However, this also produces less LW radiation, as shown in the bottom panel, dissociating H_2 more weakly.

Changing $L_{X,<2{\rm keV}}^{(\rm III)}/{\rm SFR}$ only impacts the relative timing of the EoH. Increasing the X-ray luminosity of the first galaxies results in a larger overlap of the EoH and EoC, as the coupling is not completed before the IGM is heated. Consequently, the GS absorption trough is shallower, and the large-scale power decreases from the increased negative contribution of the cross-power in these two fields (e.g. Pritchard & Furlanetto 2007; Mesinger et al. 2013; Schneider et al. 2021).

Each of the parameters impacts the signal differently as a function of redshift and scale, which may allow us to distinguish between them. However, in order to forecast parameter uncertainties, one has to capture the correlations between them, for instance through an MCMC (Greig & Mesinger 2015) or Fisher matrix (Mason et al., in preparation). We leave this question for future work. We note that the expected SNRs for the OPT model are similar to the EOS ones reported in Section 3. That is because the OPT model shows slightly

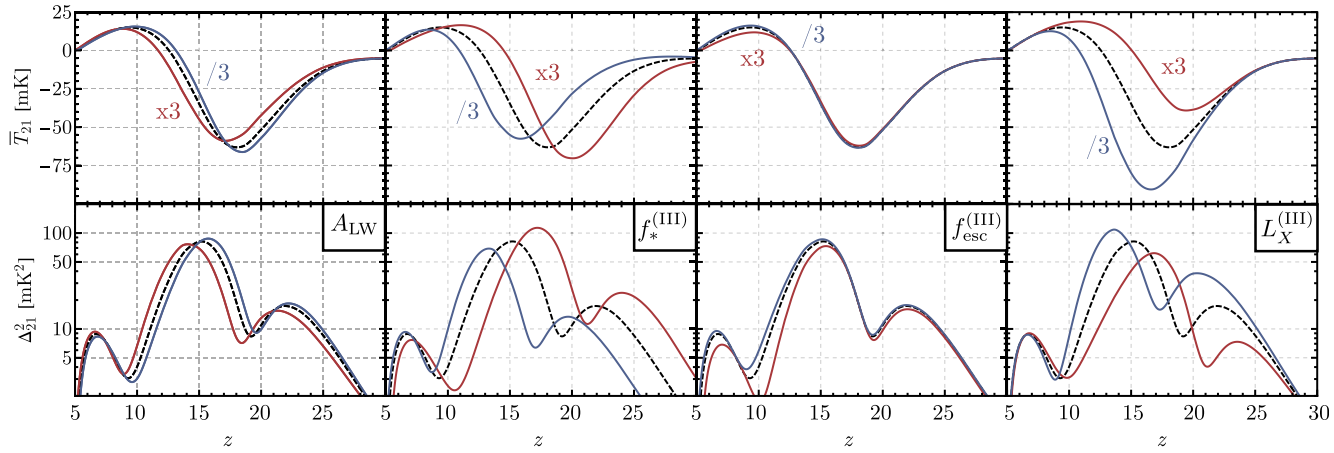

Figure 17. The effect of varying four Pop III parameters on the 21-cm global signal (top) and power spectrum (bottom, at $k = 0.23\,{\rm Mpc}^{-1}$). These parameters encode the strength of LW feedback ($A_{\rm LW}$), the stellar efficiency ($f_*^{\rm (III)}$) and escape fraction ($f_{\rm esc}^{\rm (III)}$) of MCGs, as well as the X-ray luminosity $L_X^{\rm (III)}$ per unit SFR of Pop III stars. Black dashed lines show our OPT fiducial model, and in each panel we indicate the parameter we vary, increasing (decreasing) it threefold in red (blue).

Table 3. Same as Table 2 but for the OPT parameters.

SNR for OPT	Total	EoR	EoH	EoC
HERA	206	193	66	31
HERA (pess.)	94	93	16	6
SKA	195	178	69	37
SKA (pess.)	99	95	25	11

larger fluctuations, though at lower frequencies where noise is larger. Table 3 contains our forecasted SNRs for the OPT parameters under each of the assumptions considered.

5 VELOCITY-INDUCED ACOUSTIC OSCILLATIONS

The last study we perform is on the unique signature of the DM-baryon relative velocities on the 21-cm fluctuations. We quantify to what extent the streaming velocities produce velocity-induced acoustic oscillations (VAOs) on the 21-cm signal in our simulations, for the first time jointly including inhomogeneous LW feedback with self-shielding. Throughout this section we will assume astrophysical parameters from the Optimistic (OPT) set, unless otherwise specified.

5.1 VAOs across cosmic dawn

The interactions between baryons and photons give rise to the well-known baryon acoustic oscillations (BAOs), which at low z are observed in the matter distribution as an excess correlation at the baryon acoustic scale (here used interchangeably with the baryon drag scale $r_{\rm drag}$; Eisenstein & Hu 1998). The dark matter, however, does not partake in these BAOs, which gives it different initial conditions than baryons at recombination. This produces a relative (or streaming) velocity between dark matter and baryons, which fluctuates spatially with the same $r_{\rm drag}$ scale, due to their acoustic origin (Tseliakhovich & Hirata 2010). In Fourier space, the power spectrum of $v_{\rm cb}$ presents large wiggles, which are inherited by the radiation fields, as regions of large relative velocity suppress the formation of the first stars (chiefly PopIII, see Section 2.2). Consequently, the 21-cm signal becomes modulated by these streaming velocities during cosmic dawn, giving rise to velocity-induced acoustic oscillations (VAOs; Dalal et al. 2010; Visbal et al. 2012; Fialkov et al. 2013; Muñoz 2019a), with the same acoustic origin as the BAOs, though sourced by velocity – rather than density – fluctuations. Muñoz (2019b) showed that these VAOs provide us with a standard ruler to measure physical cosmology during cosmic dawn, independently of galaxy astrophysics.

Until recently it was not known how the feedback from $v_{\rm cb}$ interacted with the LW dissociation of molecular hydrogen. As we showed in Section 2, however, recent hydrodynamical simulations from Kulkarni et al. (2021) and Schauer et al. (2021) indicate that for the regime of interest ($J_{21} \leq 1$) these two processes act coherently. Furthermore, self-shielding in the first galaxies produces weaker LW feedback, and thus a larger impact of the relative velocities. Together, these two effects give rise to sizable VAOs, as we now show.

5.1.1. Slices

We begin by showing the impact of $v_{\rm cb}$ directly on the 21-cm maps. For that we compare a standard simulation (with OPT parameters) against one with no fluctuating $v_{\rm cb}$ (achieved by setting `FIX_VAVG = True` in `21-cm FAST`). The latter simulation just uses a homogeneous value of $v_{\rm cb} = v_{\rm avg} \approx 26$ km s^{-1}, corresponding to the mean of its distribution. The reason for this choice, rather than setting $v_{\rm cb} = 0$, is that the background evolution in the latter case would be significantly different (see e.g. Fig. 10), making it difficult to compare results at a fixed redshift.

We plot slices (1.5 Mpc thick) through our simulations at $z = 11$ (during the EoH) in Fig. 18. The slice through the relative-velocity field clearly shows large-scale acoustic structure, with islands of large $v_{\rm cb}$ separated by roughly $r_{\rm drag} \approx 150$ Mpc. In contrast, the matter field (δ) has power on all visible scales, down to our cell size. We also show the 21-cm map resulting from our two simulations with and without fluctuating $v_{\rm cb}$ (but with otherwise identical OPT parameters). Regions of large $v_{\rm cb}$ have a colder IGM, as they form fewer stars, and thus emit fewer X-rays. In order to illustrate this effect, we zoom into a patch 100 Mpc in size near a region of large $v_{\rm cb}$, where the full-physics simulation clearly presents deeper absorption correlated with the velocity map.

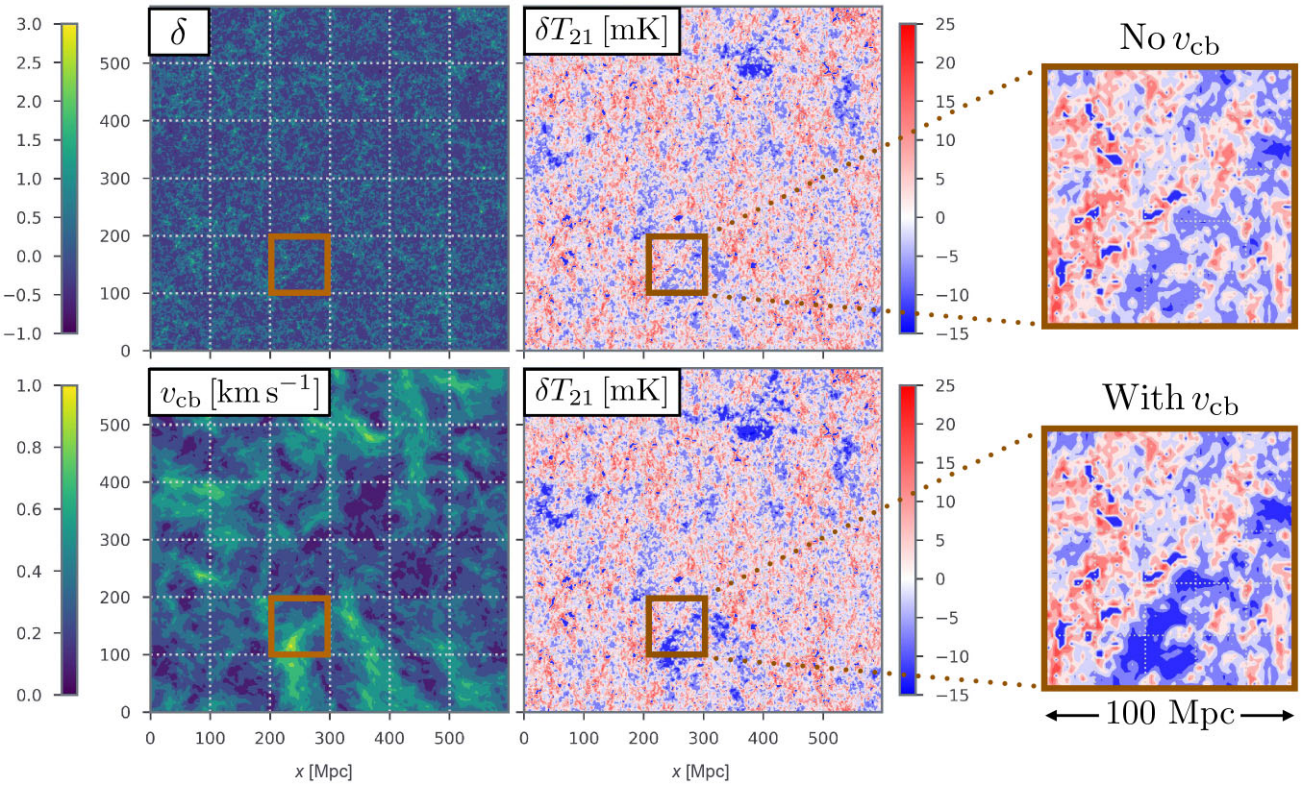

Figure 18. Effect of relative velocities on the 21-cm signal with our OPT parameters and the most up-to-date feedback prescriptions. We show a slice through our simulations, 1.5-Mpc deep and 600 Mpc on a side, at $z = 11$, where different panels show different quantities. Top left shows the matter density, and bottom left the DM-baryon relative velocity. The two central panels plot the 21-cm brightness temperature, on the top without fluctuating relative velocities (i.e. $v_{cb} = v_{avg}$), and in the bottom with the full v_{cb} effect. We also show a zoom-in (100 by 100 Mpc) region of large relative velocity on the right, where the suppressive effect of v_{cb} on the first galaxies – and thus on T_{21} – is readily apparent.

We now move on to study the effect of v_{cb} during other cosmic eras. In Fig. 19, we show a 100 Mpc zoom-in of our simulations, at the same location as in Fig. 18. Rather than showing maps of δT_{21} with and without VAOs, we plot the difference (Diff $\equiv \delta T_{21}^{\rm full} - \delta T_{21}^{\rm no\,VAO}$) between the two cases, which allows for a closer comparison, at three redshift snapshots. The first is at $z = 7$, during the EoR, where the effect of the relative velocities is rather small, affecting the signal at the ∼1–2 mK level. The second is at $z = 15$, at the peak of heating, and shows a large impact of v_{cb}, causing Diff ≈±5 mK, with the largest differences taking place in the lowest-v_{cb} regions, which heated more slowly. The last snapshot is at $z = 20$, which is during the EoC and where v_{cb} impacts the signal moderately, but in the opposite direction (as fewer photons produces less coupling, and thus more positive δT_{21}). As is clear from Fig. 18, the profile of the relative velocity (left-hand panel) is smeared when observed in the 21-cm signal, due to photon propagation. This is especially true in the $z = 20$ panel, where the difference has a homogeneous value of ∼+2 mK in the entire (100 Mpc) zoom-in region. This is because the photons just redward of Lyman β that drive WF coupling have mean free paths comparable to the 100-Mpc scale of these zoom-ins. Below we provide a simple analytical expression for the 21-cm PS including VAOs and accounting for such photon diffusion via window functions.

5.1.2. *Power spectrum*

The simulation slices studied above give us an idea of the impact of the relative velocities on the 21-cm signal at different epochs. We now calculate the 21-cm PS as a function of k, quantifying the observable signature of the VAOs. We plot this observable from our simulations in Fig. 20 at the same redshifts as were shown in Figs 18 and 19. The amplitude of those power spectra trace the overall redshift evolution that we studied in Section 3. However, more interestingly from the point of view of VAOs is the shape of the PS with k. The simulation data points show marked acoustic oscillations (i.e. wiggles) at $k = 0.05$–$0.5\,{\rm Mpc}^{-1}$, inherited from the v_{cb} fluctuations. These VAOs are most pronounced during the X-ray heating era, increasing the power spectrum by an $\mathcal{O}(1)$ factor both at $z = 11$ and $z = 15$. They also appear during the EoC, at $z = 20$, and to a much lesser degree in the EoR at $z = 7$ (though we do not consider the effect of v_{cb} on ionizing sinks, as described in Cain et al. (2020) and Park et al. (2021), which may enhance the late-time VAOs).

The relative velocity $\mathbf{v}_{cb}$ is a vector field, so due to isotropy it can only affect observables through v_{cb}^2 to first order. We define the VAO shape $\Delta^2_{v_{cb}}$ to be the power spectrum of

$$\delta_v = \sqrt{\frac{3}{2}}\left(\frac{v_{cb}^2}{v_{rms}^2} - 1\right). \tag{26}$$

This quantity has unit variance, zero mean, and is redshift independent. In Muñoz (2019a), we showed that the shape of the VAOs is unaltered by the complex astrophysics of cosmic dawn,[11] although

[11]This is not true for all scenarios, as for instance the sharp cutoffs in the primordial-black hole accretion model of Jensen & Ali-Haïmoud (2021) do not always follow the VAO shape.

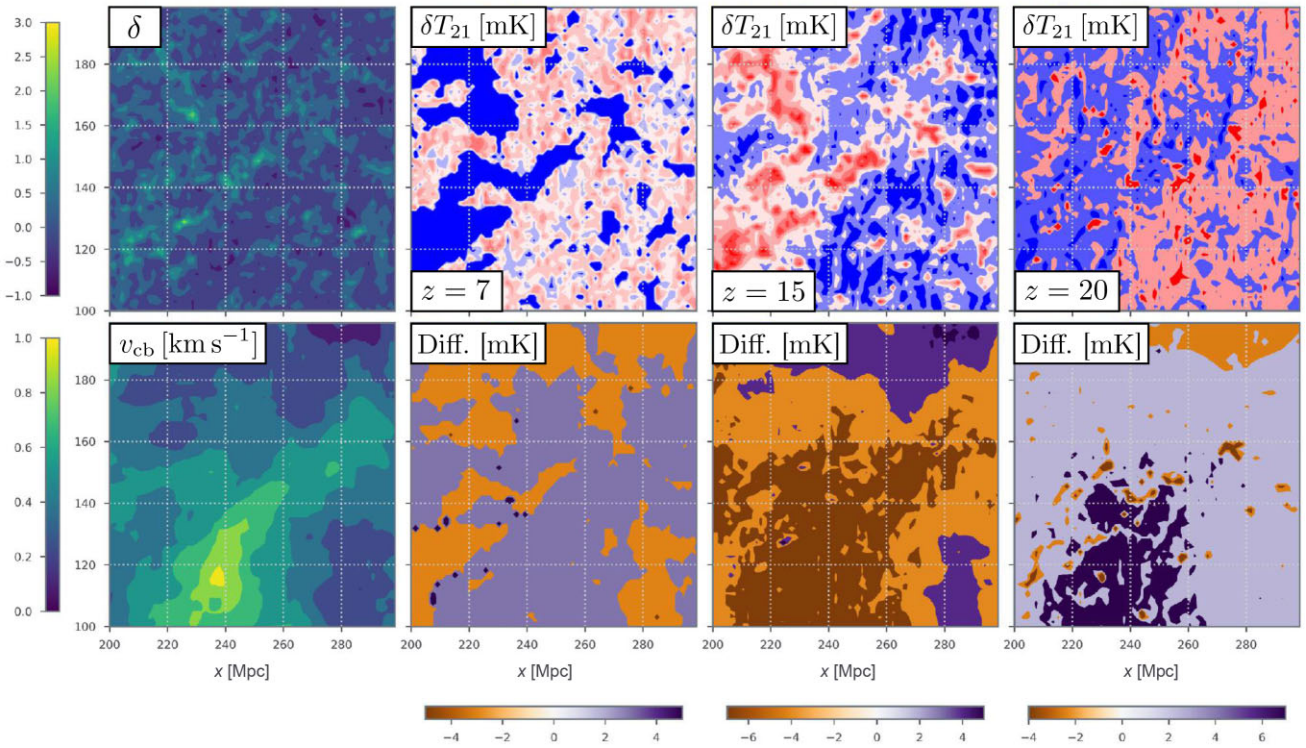

Figure 19. Zoom-in slice, 100 Mpc on a side and 1.5 Mpc in depth, from the same region as Fig. 18. We show the zoomed-in density δ and relative velocity $v_{\rm cb}$ at $z = 11$ in the left two panels. The rest of top panels show the 21-cm fluctuations δT_{21} for no VAOs ($v_{\rm cb} = v_{\rm avg}$), whereas the bottom panels show its difference with the full (i.e. with VAO) case, defined as Diff $= \delta T_{21}^{\rm full} - \delta T_{21}^{\rm no\,VAO}$. The effect of VAOs is subtle during the EoR ($z = 7$, second column), as differences are at the $\lesssim$2 mK level, but more noticeable during the EoH ($z = 15$, third column) and the EoC ($z = 20$, fourth column).

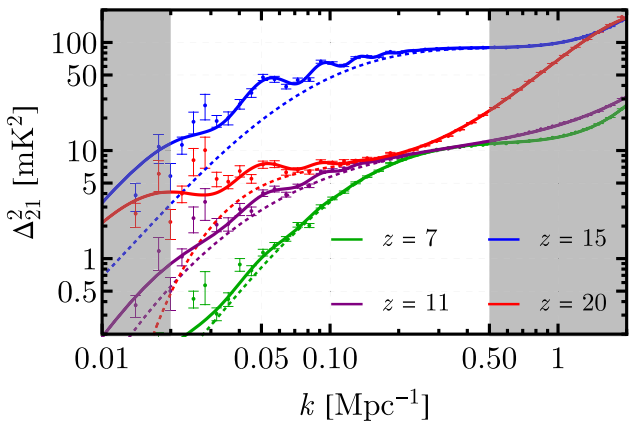

Figure 20. The 21-cm power spectrum as a function of wavenumber k at four redshifts z. The data-points show our simulation results (and Poisson noise) for the OPT parameters, and the lines present fits obtained using equation (27). The solid line contains VAOs, whereas the dashed line does not (i.e. it has $b_{v_{\rm cb}} = 0$), which has lower power at large scales and no wiggles. Simulation data-points in the grey shaded regions have not been included in the fit. The VAOs are most obvious during the EoH ($z \approx 10$–15), are somewhat visible during the EoC ($z \gtrsim 15$, though suppressed at high k), and very small during the EoR $z \lesssim 10$.

its amplitude is damped if the X-ray or UV photons that affect the 21-cm signal travel significant distances (comparable to $1/k$). Thus, not only does the amplitude of the VAOs change between eras, but also the k range where they are visible. This is clear from Fig. 20, as the $z = 15$ power spectrum has ∼3–4 visible wiggles, whereas at $z =$ 20 only 2 can be distinguished. That is because during the EoC the mean-free path of the relevant Lyman band photons is rather large (∼100 Mpc; Dalal et al. 2010), whereas during the X-ray heating era it is much shorter for realistic SEDs (Pacucci et al. 2014; Das et al. 2017). This is especially true for our OPT set of parameters, which has an optimistic value of $E_0 = 0.2$ keV and thus X-rays travel shorter distances. For the EOS parameter set on the other hand, we set $E_0 = 0.5$ keV (see Das et al. 2017), resulting in longer X-ray mean free path and thus more damped VAOs (c.f. Fig. 13, where only 2–3 wiggles are apparent).

In order to analytically model the VAOs we follow the approach of Muñoz (2019a,b, see also Hotinli et al. 2021), and use the fact that density- and $v_{\rm cb}$-sourced fluctuations are uncorrelated to first order to write

$$\Delta^2_{21} = \mathcal{P}_{\rm nw}(k) + b^2_{v_{\rm cb}} W_i^2(k) \Delta^2_{v_{\rm cb}}(k), \tag{27}$$

where $\Delta^2_{v_{\rm cb}}$ is the power spectrum of δ_v in equation (26) and contains the VAO shape, $b_{v_{\rm cb}}$ is a bias factor that determines its amplitude, and W_i is a window function that accounts for photon propagation. The $\mathcal{P}_{\rm nw}(k)$ 'no-wiggle' term, instead, accounts for the usual density-sourced 21-cm fluctuations, and we model it as a simple 4th order polynomial,

$$\log \mathcal{P}_{\rm nw}(k) = \sum_{j=0}^{4} c_j \left[\log(k)\right]^j, \tag{28}$$

which suffices to capture its behaviour in the region of interest ($k =$ 0.02–0.5 Mpc^{-1}).

For the 'wiggle' VAO part we know $\Delta^2_{v_{\rm cb}}$, but need to find both the window function W_i that accounts for damping of VAOs, and the

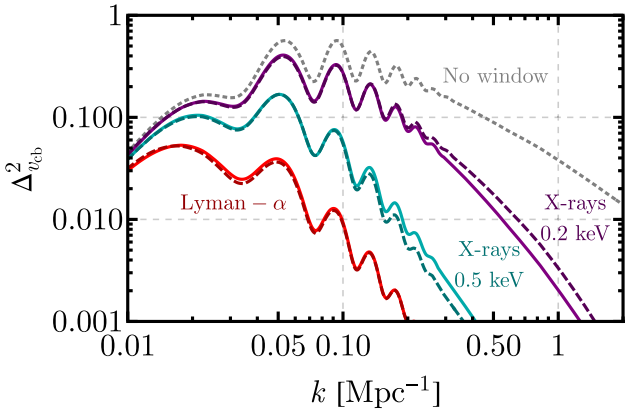

Figure 21. Relative-velocity power spectrum, from equation (26), in the case that it is not modulated by any window function (grey dotted), as well as damped by the mean free path of X-rays with a cutoff at 0.2 keV (purple), 0.5 keV (teal), and of the UV photons that produce WF coupling upon re-entering the Lyman α transition (red). For these three cases, dashed lines show the numeric result from Muñoz (2019a), whereas the solid lines follow the simpler fit presented in equation (29).

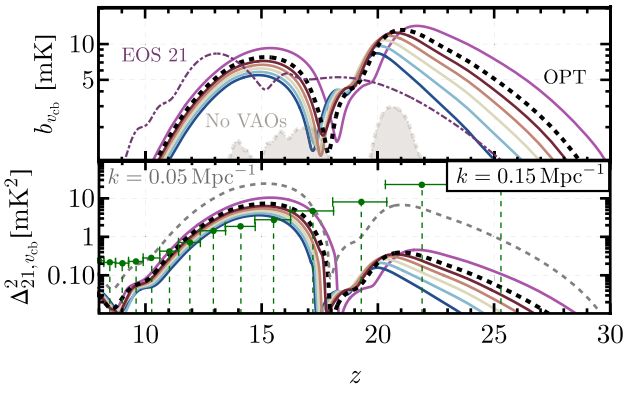

Figure 22. Size of the VAOs under different assumptions. As before, the black dashed line shows our fiducial SHMR for MCGs, with an index $\alpha_*^{(III)} = 0$, whereas the red-blue and pink lines represent different values of that index, following the same convention as Fig. 16. The top panel shows the velocity bias $b_{v_{cb}}$, defined in equation (27), where the shaded brown region is the result of fitting a simulation with no VAOs (fixing $v_{cb} = v_{avg}$), and can be taken as an error estimate of the fitting procedure. The purple dash–dotted line shows the results for the EOS parameters, rather than OPT. The bottom panel shows the VAO-only power spectrum at $k = 0.15\,\mathrm{Mpc}^{-1}$, in the range observable by HERA (whose noise is shown in green for $k = 0.05$–$0.15\,\mathrm{Mpc}^{-1}$). We additionally show the power in our fiducial ($\alpha_*^{(III)} = 0$) case at $k = 0.05\,\mathrm{Mpc}^{-1}$, as a dashed grey line, which grows significantly for the EoC ($z > 17$) as VAOs are less damped at smaller k during that epoch.

bias $b_{v_{cb}}$ that parametrizes their amplitudes. Let us begin with the window function.

We follow the approach of Muñoz (2019a) and define separate window functions $W_i(k)$ for the EoC ($i = \alpha$) and the EoH ($i = X$). Rather than computing them numerically, as is done in Dalal et al. (2010) and Muñoz (2019a), here we use a parametrized form that provides a good fit across the entire range of interest. We write

$$W_i(k) = \left[\frac{1}{1 + (k/k_{\mathrm{cut},i})^{\beta_i}}\right]^{1/\beta_i}, \tag{29}$$

which has two free parameters (β_i and $k_{\mathrm{cut},i}$) for each era, fitted to the results of Muñoz (2019a) but kept independent of z otherwise. We find that for Lyman α photons $\beta_a = 2$ and $k_{\mathrm{cut},a} = 0.015\,\mathrm{Mpc}^{-1}$ provide an excellent fit. For X-rays, the damping depends on the assumed energy cutoff scale (i.e. the minimum X-ray energy E_0 escaping the ISM of host galaxies). First, for $E_0 = 0.2$ keV (as set in our OPT parameters), a good fit is provided by $\beta_X = 1$ and $k_{\mathrm{cut},X} = 0.3\,\mathrm{Mpc}^{-1}$. Secondly, when setting $E_0 = 0.5$ keV (for the EOS fiducial) the X-rays have longer mean free paths, and we find $\beta_X = 1.5$ and $k_{\mathrm{cut},X} = 0.04\,\mathrm{Mpc}^{-1}$. We show the VAO power spectrum in Fig. 21 multiplied by each of these window functions, together with the numerical result from Muñoz (2019a), finding good agreement. This figure also shows that, as expected, longer travel distances yield more suppression of VAO amplitudes. The Lyman α VAOs are more damped than X-rays with $E_0 = 0.5$ keV, which in turn are more damped than X-rays with a lower energy cutoff at $E_0 = 0.2$ keV. Numerically, at $z = 15$ the distance a Lyman β photon travels until entering the Lyman α resonance is roughly 300 Mpc comoving, whereas the mean-free path of X-rays is a significantly shorter 30 Mpc for $E_0 = 0.5$ keV, or 3 Mpc for 0.2 keV (McQuinn 2012). As a consequence, these latter cases have higher $k_{\mathrm{cut},i}$, and a shallower suppression index β_i. We emphasize that the parameters of this fit would technically vary with z, and have not been fit to high precision, but instead to round numbers, as that suffices for our purposes of studying the detectability of VAOs and their extraction from simulated power spectrum data.

The amplitude of the VAOs, parametrized in our analytical PS expression through the bias $b_{v_{cb}}$, depends on the astrophysics driving the 21-cm signal at any given epoch. Star formation feedback from streaming velocities preferentially impacts smaller scales, and thus MCGs are more affected than ACGs (though see Section 2 for their impact on ACGs). As a consequence, $b_{v_{cb}}$ is larger (i.e. with more prominent VAOs) for models in which the SFRD is driven by the smallest haloes. In Fig. 20, we assume the optimistic (OPT) parameters for the MCG SFR from Table 1, and thus VAOs are evident during both the EoH and EoC.

We fit for the bias parameter $b_{v_{cb}}$ for each redshift independently over the k-ranges shown in white in Fig. 20. The results are shown in Fig. 22. The amplitude of VAOs has two peaks, corresponding to the EoC (at $z \sim 20$ for our OPT parameters) and the EoH ($z \sim 15$), and all but vanishes in the transition between the two, as the effect of v_{cb} goes in opposite directions between these two eras, producing less coupling at earlier times (and thus higher T_{21}), and less heating at late times (lower T_{21}). We also show $b_{v_{cb}}$ for our EOS fiducial (*AllGalaxies*) simulation in that Figure, which shows somewhat smaller VAOs, delayed to later times; as well as a null test $b_{v_{cb}}$ for a simulation with no VAOs as an error-bar estimation of our fitting procedure. For comparison, the HERA Collaboration (2022) found that $b_{v_{cb}} < \{50, 180\}$ mK at 95 per cent CL, using their phase-1 limits at $z = \{8, 10\}$. These data only cover lower redshifts, where VAOs are not expected to be important (c.f. Fig. 22), but they highlight the need for further sensitivity to reach the level of VAOs ($b_{v_{cb}} \approx 10$ mK) predicted in our models.

In the bottom panel of Fig. 22, we plot the v_{cb}-only component of the 21-cm power spectrum, defined as $\Delta^2_{21,v_{cb}} = b^2_{v_{cb}} W_i^2(k) \Delta^2_{v_{cb}}(k)$, at a scale $k = 0.15\,\mathrm{Mpc}^{-1}$ (roughly corresponding to a 'sweet spot' in terms of foreground contamination and thermal noise for interferometers; e.g. Greig et al. 2020a; The HERA Collaboration 2022; Tingay et al. 2013; van Haarlem et al. 2013). This VAO power is relatively high during the EoH, reaching $\Delta^2_{21,v_{cb}} \approx 10$ mK^2. During the EoC, however, it only has values $\Delta^2_{21,v_{cb}} \approx 0.5$ mK^2, as the photon propagation in the latter strongly suppresses large-k fluctuations. To illustrate this point, we also plot the

VAO-only power for $k = 0.05\,\mathrm{Mpc}^{-1}$ (where the deepest LOFAR limits lie Mertens et al. 2020) in that Figure, which grows by nearly two orders of magnitude during the EoC (and one during the EoH), showing that reaching lower k by careful foreground cleaning is ideal for detecting acoustic wiggles in the high-z 21-cm signal. We predict a smaller VAO power across all of cosmic dawn than our previous work. In Muñoz (2019a) we had found $\Delta^2_{21,v_{\rm cb}} \approx 50$ mK^2 during the EoH, a factor of a few larger. Part of the reason is the inclusion of inhomogeneous LW feedback, which tends to suppress VAOs (Fialkov et al. 2013). The largest factor, however, is the new parametrization of the SFRD (see equations 1,7). In Muñoz (2019a), we considered a mass-independent SHMR shared for PopII and PopIII stars (i.e. $\alpha_*^{(i)} = 0$ for $i =$ II and III), which produces a much faster evolution of CD and larger 21-cm fluctuations (see discussion in Section 3). With the more-realistic SHMR considered here both the overall 21-cm PS and the VAOs are smaller, so VAOs are still an $\mathcal{O}(1)$ component of the large-scale 21-cm power spectrum in Fig. 20.

5.2 VAOs and the SHMR of PopIII hosts

So far we have shown VAOs in simulations with either our OPT and EOS parameter sets. Given our lack of knowledge about cosmic dawn, however, the first galaxies could have much different parameters than we expected. We now perform a brief exploratory study of how the amplitude of the VAOs can be used to learn about the astrophysics of cosmic dawn.

We focus on the slope of the SHMR for MCGs, parametrized with $\alpha_*^{(\rm III)}$, which we showed in the previous section has a very modest impact on the redshift dependence of the PS (at fixed k) and the GS. Here, we study its impact on the VAO component of the PS, shown in Fig. 22 for the same values of $\alpha_*^{(\rm III)}$ as in Fig. 16. We see that steeper SHMRs (larger $\alpha_*^{(\rm III)}$) suppress the VAO amplitude, especially at high z. This is understandable since steeper SHMRs decrease the relative contribution of the smallest haloes to the SFRD, and these smallest haloes are the most sensitive to the streaming velocities. Interestingly, the impact of $\alpha_*^{(\rm III)}$ on the VAOs component of the power appears more noticeable than in the overall 21-cm power spectrum or global signal (c.f. Fig. 16). Therefore, the amplitude of VAOs can provide a cleaner view of the halo–galaxy connection of MCGs.

We also study variations of the amplitude $A_{\rm LW}$ of the LW feedback. We find that increasing or decreasing $A_{\rm LW}$ by a factor of up to 3 does not change the amplitude of the VAOs, only its z dependence. This is because the LW and $v_{\rm cb}$ feedback effects multiply coherently, so they are rather independent. Given that the 21-cm GS and the complete PS amplitude are also insensitive to $A_{\rm LW}$ (see Fig. 17), the best avenue for studying this parameter may be further hydrodynamical simulations, instead of inferring it from 21-cm data.

5.3 Detectability

The VAOs that we study here have been shown to be a robust standard ruler during cosmic dawn, allowing 21-cm interferometers to measure the cosmic expansion rate at $z \sim 10$–20 (Muñoz 2019b). However, we would first need to detect them.

As opposed to Section 3, where we considered the entire 21-cm power spectrum, here we forecast SNRs for the $\Delta^2_{21,v_{\rm cb}}$ component. For that we use the same noise as before, which includes the cosmic variance from the full Δ^2_{21} signal. This noise is shown in Fig. 22 along with the VAO-only power spectrum. We find a SNR $= 5$ for the EOS parameters assuming 1080 h of HERA data at moderate foregrounds. For the OPT parameters, instead, we find more optimistic estimates, with SNR $= 9$. In both cases, the SNR is only above unity over the range $z \approx 10$–15, showing that the EoH is the most promising epoch to detect VAOs, and thus to measure $H(z)$ (Muñoz 2019b).

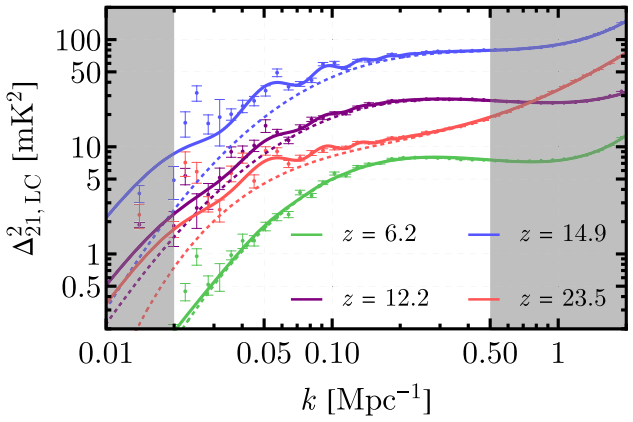

Figure 23. Power spectra in the light-cone (i.e. including LoS effects) at four bins marked by the central redshift, where each bin has an LoS comoving width of 383 Mpc, as well as their fits using equation (27). This figure shows that VAOs are still present in the light-cone (LC) power spectra.

5.4 VAOs in the lightcone

All work on VAOs thus far has been on co-eval boxes (i.e. at fixed z). In reality, however, 21-cm fluctuations are measured in the light-cone, as the fluctuations along the line-of-sight (LoS) direction evolve with z. This is particularly important for using VAOs as a standard ruler, as mainly LoS modes are observed by interferometers, which are then used to measure $H(z)$.

It is expected that LoS effects slightly change the large-scale 21-cm power (Datta et al. 2012; La Plante et al. 2014; Ghara, Datta & Choudhury 2015; Greig & Mesinger 2018). In order to include these effects we divide our light-cone, which is 600 Mpc on a side and 3830 Mpc in length, into 10 blocks (each 383 Mpc along the LoS), and compute the power spectrum in each of them. We show the resulting full-light-cone 21-cm power spectra in Fig. 23, where the VAOs are still clearly apparent (with larger Poisson noise from the simulations as each z box corresponds to a smaller comoving volume). While a full comparison of light-cone and co-eval boxes is beyond the scope of this work, we find that during the EoH the bias $b_{v_{\rm cb}}$ is reduced by 20 per cent, showing a small but not negligible LoS effect on the amplitude of VAOs, though not on their shape. This is an important cross-check for using VAOs as a standard ruler. For a brief study of how to measure VAOs without Poisson variance from the simulations we encourage the reader to visit Appendix C.

6 DISCUSSION AND CONCLUSIONS

The first generation of PopIII stars heralded the transition from the dark ages to the cosmic dawn. In this work, we have improved the treatment of these stars in the public code `21cmFAST`, including the combined impact on star formation from baryon-DM streaming velocities ($v_{\rm cb}$) and the inhomogeneous LW background. In our model, PopIII stars are hosted in molecular-cooling galaxies (MCGs, with halo masses $M_{\rm h} < M_{\rm atom} \sim 10^{7-8}\,\mathrm{M}_\odot$), whereas PopII stars form in atomic-cooling galaxies (ACGs, with masses above $M_{\rm atom}$). Thus, PopIII stars dominate the photon budget in the early universe, and are expected to set the timing of the cosmic-dawn 21-cm signal at $z \sim 10$–20. Later on, however, feedback and the natural apearence

Table 4. Table with the simulations that we make publicly available. The EOS fiducial has a more conservative SHMR for MCGs compared to ACGs, as opposed to our Optimistic (OPT) fiducial (see Table 1 for parameter values). All simulations have a resolution of 1.5 Mpc per cell, and an asterisk denotes that we make full light-cones available, in addition to global quantities and power spectra.

Name	PopII parameters	PopIII parameters	Size (Mpc)
`EOS2021* (AllGalaxies)`	EOS 2021 (EOS)	EOS	1500
`600_EOS`	EOS	EOS	600
`600_novel`	EOS	EOS ($A_{v_{cb}} = 0$)	600
`600_noMINI`	EOS	None	600
`600ptX`	Optimistic (OPT)	OPT ($\alpha_*^{(III)} = X$, for -0.2–0.5)	600
`600alwY`	OPT	OPT ($A_{LW} = Y$)	600
*400_i_hi**	OPT	OPT ($\theta_i \times 3$)	400
*400_i_lo**	OPT	OPT ($\theta_i/3$)	400

of heavier haloes will make MCGs subdominant, and PopII stars are expected to drive cosmic reionization, at $z \sim 5$–10.

Many questions remain about the formation of the first galaxies. As such, here we implement flexible models that account for two distinct (PopII and III) stellar populations with different SHMRs, building upon Park et al. (2019), Muñoz (2019a), and Qin et al. (2020a). We provide generic fitting formulae for the impact of LW and v_{cb} feedback (in Section 2), and calibrate them with results from state-of-the-art hydrodynamical simulations. This allows us to generate a new EOS 2021 model covering the evolution of the 21-cm signal across cosmic dawn and reionization, which encapsulates our current knowledge of these epochs. We have dubbed this model *AllGalaxies*, and it enhances the previously available *Bright* and *FaintGalaxies* (from EOS 2016) by including PopIII-hosting MCGs. The parameters of this *AllGalaxies* model are chosen to give rise to late reionization (finishing at $z \approx 5.5$, as expected from recent Lyman α forest data), and its CMB optical depth is $\tau_{CMB} = 0.063$, in line with recent determinations from *Planck*. The 21-cm signal in our *AllGalaxies* simulation is shallower (only reaching $\overline{T}_{21} \approx -75$ mK during cosmic dawn) than in the previous EOS models. This is due to both the inclusion of MCGs and a steeper SHMR for ACGs, the later being required to match UVLF observations. As a consequence, both the expected 21-cm global signal and its fluctuations will be more difficult to detect (see also Mirocha et al. 2017; Park et al. 2019). Nevertheless, we expect both the HERA and SKA interferometers to reach a 21-cm power spectrum detection of this model at an SNR $\approx$200 with 1000 h of integration. We make public the detailed light-cones of this model, as well as associated visualizations.

We also performed an exploratory study of how PopIII stars affect the cosmological 21-cm signal. We have found that for the redshifts of interest for MCGs ($z \gtrsim 12$), v_{cb} feedback likely dominates over LW feedback (cf. Fig. 5). As a consequence, the amplitude A_{LW} of LW feedback only has a modest impact on the 21-cm signal. Similarly, the signal is not sensitive to the escape fraction $f_{esc}^{(III)}$ of ionizing photons from MCGs, as MCGs do not significantly contribute to reionization in our model. On the other hand, the star formation efficiency and the X-ray luminosities of MCGs do impact the 21-cm signal significantly.

The streaming velocities v_{cb} fluctuate spatially with an acoustic signature inherited from recombination. As a consequence, the distribution of the first galaxies (and thus the 21-cm signal) shows velocity-induced acoustic oscillations (VAOs): large wiggles in their power spectrum at $k \lesssim 0.1$ Mpc^{-1}. We showed that VAOs are present and detectable even when including inhomogeneous LW feedback, and considering light-cone effects. This will allow us to use the 21-cm power spectrum as a standard ruler during cosmic dawn. Moreover, the amplitude of the 21-cm VAO oscillations can be used to study the SHMR of MCGs. The slope of the SHMR can provide insight about the stellar content of MCGs and the associated feedback mechanisms; without VAOs, this important quantity would be very difficult to detect.

Our results and public simulations can be used to guide 21-cm observing strategies and data pipelines. With our current state of knowledge we expect the 21-cm power spectrum to be detected at high significance by upcoming interferometric observations. Such a detection will provide us with a new window on the stellar and energy content of our cosmos at unprecedented early times.

ACKNOWLEDGEMENTS

We are grateful to Greg Bryan, Daniel Eisenstein, and Jordan Mirocha for enlightening discussions. JBM is supported by a Clay fellowship at the Smithsonian Astrophysical Observatory. AM acknowledges funding from the European Research Council (ERC) under the European Union's Horizon 2020 research and innovation programme (grant agreement No 638809 – AIDA). The results presented here reflect the authors' views; the ERC is not responsible for their use. Parts of this research were supported by the Australian Research Council Centre of Excellence for All Sky Astrophysics in 3 Dimensions (ASTRO 3D), through project number CE170100013. We gratefully acknowledge computational resources of the Center for High Performance Computing (CHPC) at Scuola Normale Superiore (SNS). This work was performed in part at the Aspen Center for Physics, which is supported by National Science Foundation grant PHY-1607611. This work was partially supported by a grant from the Simons Foundation. CAM acknowledges support by the VILLUM FONDEN under grant 37459 and from NASA Headquarters through the NASA Hubble Fellowship grant *HST*-HF2-51413.001. A awarded by the Space Telescope Science Institute, which is operated by the Association of Universities for Research in Astronomy, Inc., for NASA, under contract NAS5-26555.

DATA AVAILABILITY

All the simulations presented in this work are freely available for download (see footnote 2). We make light-cones from the *AllGalaxies* simulation (initial conditions, perturbed densities, relative velocities, spin and kinetic temperatures, ionization fractions, and 21-cm brightness temperatures) publicly available. In addition to the *AllGalaxies* simulation (1.5 Gpc in size), we share the output of the simulations used in Section 3 (which are either 600 or 400 Mpc in size, at the same resolution). We compile the names of the simulations, and their parameters, in Table 4.

REFERENCES

Abazajian K. N. et al., 2016, preprint (arXiv:1610.02743)
Abel T., Bryan G. L., Norman M. L., 2002, Science, 295, 93
Ade P. et al., 2019, J. Cosmol. Astropart. Phys., 02, 056
Aghanim N. et al., 2020, A&A, 641, A6
Ahn K., Shapiro P. R., 2021, ApJ, 914, 44
Atek H. et al., 2015, ApJ, 814, 69
Atek H., Richard J., Kneib J.-P., Schaerer D., 2018, MNRAS, 479, 5184
Barkana R., 2018, Nature, 555, 71
Barkana R., Loeb A., 1999, ApJ, 523, 54
Barkana R., Loeb A., 2001, Phys. Rep., 349, 125
Barkana R., Loeb A., 2004, ApJ, 609, 474
Barkana R., Loeb A., 2005, ApJ, 626, 1
Beardsley A. P. et al., 2016, ApJ, 833, 102
Becker G. D., Bolton J. S., Madau P., Pettini M., Ryan-Weber E. V., Venemans B. P., 2015, MNRAS, 447, 3402
Behroozi P. S., Wechsler R. H., Conroy C., 2013, ApJ, 770, 57
Behroozi P., Wechsler R. H., Hearin A. P., Conroy C., 2019, MNRAS, 488, 3143
Bond J. R., Cole S., Efstathiou G., Kaiser N., 1991, ApJ, 379, 440
Bosman S. E. I., Fan X., Jiang L., Reed S., Matsuoka Y., Becker G., Haehnelt M., 2018, MNRAS, 479, 1055
Bouwens R. J. et al., 2014, ApJ, 793, 115
Bouwens R. J. et al., 2015, ApJ, 803, 34
Bouwens R. J. et al., 2016, ApJ, 830, 67
Bouwens R. J. et al., 2021, AJ, 162, 47
Bowman J. D., Rogers A. E. E., Monsalve R. A., Mozdzen T. J., Mahesh N., 2018, Nature, 555, 67
Bromm V., Larson R. B., 2004, ARA&A, 42, 79
Cain C., D'Aloisio A., Iršič V., McQuinn M., Trac H., 2020, ApJ, 898, 168
Choudhury T. R., Paranjape A., Bosman S. E. I., 2021, MNRAS, 501, 5782
Cohen A., Fialkov A., Barkana R., 2018, MNRAS, 478, 2193
Dalal N., Pen U.-L., Seljak U., 2010, J. Cosmol. Astropart. Phys., 1011, 007
Das A., Mesinger A., Pallottini A., Ferrara A., Wise J. H., 2017, MNRAS, 469, 1166
Datta K. K., Mellema G., Mao Y., Iliev I. T., Shapiro P. R., Ahn K., 2012, MNRAS, 424, 1877
Dayal P., Ferrara A., Dunlop J. S., Pacucci F., 2014, MNRAS, 445, 2545
de Belsunce R., Gratton S., Coulton W., Efstathiou G., 2021, MNRAS, 507, 1072
DeBoer D. R. et al., 2017, PASP, 129, 045001
Dewdney P. et al., 2016, Technical report, SKA1 System baseline design V2. SKA office
Draine B. T., Bertoldi F., 1996, ApJ, 468, 269
Eastwood M. W. et al., 2019, AJ, 158, 84
Eisenstein D. J., Hu W., 1998, ApJ, 496, 605
Ewall-Wice A., Chang T.-C., Lazio J., Doré O., Seiffert M., Monsalve R. A., 2018, ApJ, 868, 63
Fialkov A., Barkana R., 2014, MNRAS, 445, 213
Fialkov A., Barkana R., Tseliakhovich D., Hirata C. M., 2012, MNRAS, 424, 1335
Fialkov A., Barkana R., Visbal E., Tseliakhovich D., Hirata C. M., 2013, MNRAS, 432, 2909
Field G. B., 1959, ApJ, 129, 536
Fragos T., Lehmer B. D., Naoz S., Zezas A., Basu-Zych A., 2013, ApJ, 776, L31
Furlanetto S. R., Oh S. P., Briggs F. H., 2006, Phys. Rep., 433, 181
Garaldi E., Kannan R., Smith A., Springel V., Pakmor R., Vogelsberger M., Hernquist L., 2021, preprint (arXiv:2110.01628)
Ghara R., Datta K. K., Choudhury T. R., 2015, MNRAS, 453, 3143
Greif T. H., White S. D. M., Klessen R. S., Springel V., 2011, ApJ, 736, 147
Greig B., Mesinger A., 2015, MNRAS, 449, 4246
Greig B., Mesinger A., 2018, MNRAS, 477, 3217
Greig B., Mesinger A., Haiman Z., Simcoe R. A., 2017, MNRAS, 466, 4239
Greig B., Mesinger A., Bañados E., 2019, MNRAS, 484, 5094
Greig B., Mesinger A., Koopmans L. V. E., 2020a, MNRAS, 491, 1398
Greig B., Trott C. M., Barry N., Mutch S. J., Pindor B., Webster R. L., Wyithe J. S. B., 2020b, MNRAS, 500, 5322
Haiman Z., Bryan G. L., 2006, ApJ, 650, 7
Heinrich C., Hu W., 2021, Phys. Rev. D, 104, 063505
Hills R., Kulkarni G., Meerburg P. D., Puchwein E., 2018, Nature, 564, E32
Hirano S., Yoshida N., Sakurai Y., Fujii M. S., 2018, ApJ, 855, 17
Hirata C. M., 2006, MNRAS, 367, 259
Hotinli S. C., Binnie T., Muñoz J. B., Dinda B. R., Kamionkowski M., 2021, Phys. Rev. D, 104, 063536
Hui L., Gnedin N. Y., 1997, MNRAS, 292, 27
Ishigaki M., Kawamata R., Ouchi M., Oguri M., Shimasaku K., Ono Y., 2018, ApJ, 854, 73
Jensen T. W., Ali-Haïmoud Y., 2021, Phys. Rev. D, 104, 063534
Johnson J. L., Greif T. H., Bromm V., 2007, ApJ, 665, 85
Jones D., Palatnick S., Chen R., Beane A., Lidz A., 2021, ApJ, 913, 7
Kannan R., Smith A., Garaldi E., Shen X., Vogelsberger M., Pakmor R., Springel V., Hernquist L., 2021, preprint (arXiv:2111.02411)
Katz H. et al., 2020, MNRAS, 494, 2200
Keating L. C., Weinberger L. H., Kulkarni G., Haehnelt M. G., Chardin J., Aubert D., 2020, MNRAS, 491, 1736
Kimm T., Katz H., Haehnelt M., Rosdahl J., Devriendt J., Slyz A., 2017, MNRAS, 466, 4826
Koopmans L. V. E. et al., 2015, Proc. Sci., The Cosmic Dawn and Epoch of Reionisation with SKA. SISSA, Trieste, PoS#1
Kulkarni G., Keating L. C., Haehnelt M. G., Bosman S. E. I., Puchwein E., Chardin J., Aubert D., 2019, MNRAS, 485, L24
Kulkarni M., Visbal E., Bryan G. L., 2021, ApJ, 917, 40
La Plante P., Battaglia N., Natarajan A., Peterson J. B., Trac H., Cen R., Loeb A., 2014, ApJ, 789, 31
Lewis J. S. W. et al., 2020, MNRAS, 496, 4342
Lidz A., Zahn O., McQuinn M., Zaldarriaga M., Hernquist L., 2008, ApJ, 680, 962
Livermore R., Finkelstein S., Lotz J., 2017, ApJ, 835, 113
Loeb A., Furlanetto S. R., 2013, The First Galaxies in the Universe. Princeton Univ. Press, Princeton
Loeb A., Zaldarriaga M., 2004, Phys. Rev. Lett., 92, 211301
Machacek M. E., Bryan G. L., Abel T., 2001, ApJ, 548, 509
Madau P., Ferguson H. C., Dickinson M. E., Giavalisco M., Steidel C. C., Fruchter A., 1996, MNRAS, 283, 1388
Mason C. A., Trenti M., Treu T., 2015, ApJ, 813, 21
Mason C. A. et al., 2019a, MNRAS, 485, 3947
Mason C. A., Naidu R. P., Tacchella S., Leja J., 2019b, MNRAS, 489, 2669
McGreer I. D., Mesinger A., D'Odorico V., 2015, MNRAS, 447, 499
McQuinn M., 2012, MNRAS, 426, 1349
McQuinn M., O'Leary R. M., 2012, ApJ, 760, 3
Mebane R. H., Mirocha J., Furlanetto S. R., 2018, MNRAS, 479, 4544
Mellema G. et al., 2013, Exp. Astron., 36, 235
Mertens F. G. et al., 2020, MNRAS, 493, 1662
Mesinger A., 2016, Understanding the Epoch of Cosmic Reionization Astrophysics and Space Science Library, Vol. 423, Springer International Publishing, Switzerland
Mesinger A., Furlanetto S., 2007, ApJ, 669, 663
Mesinger A., Ferrara A., Spiegel D. S., 2013, MNRAS, 431, 621
Mesinger A., Furlanetto S., Cen R., 2011, MNRAS, 411, 955
Mesinger A., Greig B., Sobacchi E., 2016, MNRAS, 459, 2342
Millea M., Bouchet F., 2018, A&A, 617, A96
Mirocha J., Furlanetto S. R., Sun G., 2017, MNRAS, 464, 1365
Mirocha J., Mebane R. H., Furlanetto S. R., Singal K., Trinh D., 2018, MNRAS, 478, 5591
Mirocha J., La Plante P., Liu A., 2021, MNRAS, 507, 3872
Muñoz J. B., 2019a, Phys. Rev. D, 100, 063538
Muñoz J. B., 2019b, Phys. Rev. Lett., 123, 131301
Muñoz J. B., Cyr-Racine F.-Y., 2021, Phys. Rev. D, 103, 023512
Muñoz J. B., Loeb A., 2018, Nature, 557, 684
Muñoz J. B., Dvorkin C., Cyr-Racine F.-Y., 2020, Phys. Rev. D, 101, 063526

Murray S. G., Greig B., Mesinger A., Muñoz J. B., Qin Y., Park J., Watkinson C. A., 2020, J. Open Source Softw., 5, 2582
Nadler E. O. et al., 2020, ApJ, 893, 48
Naidu R. P., Tacchella S., Mason C. A., Bose S., Oesch P. A., Conroy C., 2020, ApJ, 892, 109
Naoz S., Yoshida N., Gnedin N. Y., 2012, ApJ, 747, 128
Naoz S., Yoshida N., Gnedin N. Y., 2013, ApJ, 763, 27
Nasir F., D'Aloisio A., 2020, MNRAS, 494, 3080
Noh Y., McQuinn M., 2014, MNRAS, 444, 503
O'Leary R. M., McQuinn M., 2012, ApJ, 760, 4
O'Shea B. W., Norman M. L., 2008, ApJ, 673, 14
O'Shea B. W., Wise J. H., Xu H., Norman M. L., 2015, ApJ, 807, L12
Ocvirk P. et al., 2020, MNRAS, 496, 4087
Oesch P. A., Bouwens R. J., Illingworth G. D., Labbé I., Stefanon M., 2018, ApJ, 855, 105
Oh S. P., Haiman Z., 2002, ApJ, 569, 558
Okamoto T., Gao L., Theuns T., 2008, MNRAS, 390, 920
Paardekooper J.-P., Khochfar S., Dalla Vecchia C., 2015, MNRAS, 451, 2544
Pacucci F., Mesinger A., Mineo S., Ferrara A., 2014, MNRAS, 443, 678
Park J., Mesinger A., Greig B., Gillet N., 2019, MNRAS, 484, 933
Park H., Shapiro P. R., Ahn K., Yoshida N., Hirano S., 2021, ApJ, 908, 96
Parsons A. R., Pober J. C., Aguirre J. E., Carilli C. L., Jacobs D. C., Moore D. F., 2012, ApJ, 756, 165
Philip L. et al., 2019, J. Astron. Instrum., 8, 1950004
Pober J. C. et al., 2013a, AJ, 145, 65
Pober J. C. et al., 2013b, ApJ, 768, L36
Pober J. C. et al., 2014, ApJ, 782, 66
Pospelov M., Pradler J., Ruderman J. T., Urbano A., 2018, Phys. Rev. Lett., 121, 031103
Price D. C. et al., 2018, MNRAS, 478, 4193
Pritchard J. R., Furlanetto S. R., 2007, MNRAS, 376, 1680
Pritchard J. R., Loeb A., 2012, Rep. Prog. Phys., 75, 086901
Qin Y. et al., 2017, MNRAS, 472, 2009
Qin Y., Mesinger A., Bosman S. E. I., Viel M., 2021b, MNRAS, 506, 2390
Qin Y., Mesinger A., Greig B., Park J., 2021a, MNRAS, 501, 4748
Qin Y., Mesinger A., Park J., Greig B., Muñoz J. B., 2020a, MNRAS, 495, 123
Qin Y., Poulin V., Mesinger A., Greig B., Murray S., Park J., 2020b, MNRAS, 499, 550
Rudakovskyi A., Mesinger A., Savchenko D., Gillet N., 2021, MNRAS, 507, 3046
Sabti N., Muñoz J. B., Blas D., 2021a, preprint (arXiv:2110.13168)
Sabti N., Muñoz J. B., Blas D., 2021b, preprint (arXiv:2110.13161)
Sabti N., Muñoz J. B., Blas D., 2021c, JCAP, 01, 010
Safranek-Shrader C., Agarwal M., Federrath C., Dubey A., Milosavljević M., Bromm V., 2012, MNRAS, 426, 1159
Schauer A. T. P. et al., 2017, MNRAS, 467, 2288
Schauer A. T. P., Glover S. C. O., Klessen R. S., Ceverino D., 2019, MNRAS, 484, 3510
Schauer A. T. P., Glover S. C. O., Klessen R. S., Clark P., 2021, MNRAS, 507, 1775
Schneider R., Ferrara A., Natarajan P., Omukai K., 2002, ApJ, 571, 30
Schneider A., Giri S. K., Mirocha J., 2021, Phys. Rev. D, 103, 083025
Sims P. H., Pober J. C., 2020, MNRAS, 492, 22
Singh S., Subrahmanyan R., Shankar N. U., Rao M. S., Girish B. S., Raghunathan A., Somashekar R., Srivani K. S., 2018, Exp. Astron., 45, 269
Skinner D., Wise J. H., 2020, MNRAS, 492, 4386
Smith A., Kannan R., Garaldi E., Vogelsberger M., Pakmor R., Springel V., Hernquist L., 2021, preprint (arXiv:2110.02966)
Sobacchi E., Mesinger A., 2013, MNRAS, 432, 3340
Sobacchi E., Mesinger A., 2014, MNRAS, 440, 1662
Sun G., Furlanetto S. R., 2016, MNRAS, 460, 417
Sun G., Mirocha J., Mebane R. H., Furlanetto S. R., 2021, MNRAS, 508, 1954
Tacchella S., Bose S., Conroy C., Eisenstein D. J., Johnson B. D., 2018, ApJ, 868, 92
Tegmark M., Zaldarriaga M., 2009, Phys. Rev. D, 79, 083530
Tegmark M., Silk J., Rees M. J., Blanchard A., Abel T., Palla F., 1997, ApJ, 474, 1
The HERA Collaboration, 2022, ApJ, 924, 51
Thoul A. A., Weinberg D. H., 1996, ApJ, 465, 608
Tingay S. J. et al., 2013, Publ. Astron. Soc. Aust., 30, e007
Trenti M., 2010, AIP Conf. Proc., 1294, 134
Tseliakhovich D., Hirata C., 2010, Phys. Rev., D82, 083520
Tseliakhovich D., Barkana R., Hirata C. M., 2011, MNRAS, 418, 906
van Haarlem M. P. et al., 2013, A&A, 556, A2
Visbal E., Barkana R., Fialkov A., Tseliakhovich D., Hirata C. M., 2012, Nature, 487, 70
Visbal E., Haiman Z., Terrazas B., Bryan G. L., Barkana R., 2014, MNRAS, 445, 107
Voytek T. C., Natarajan A., Jáuregui García J. M., Peterson J. B., López-Cruz O., 2014, ApJ, 782, L9
Wang F. et al., 2020, ApJ, 896, 23
Wechsler R. H., Tinker J. L., 2018, ARA&A, 56, 435
Whitler L. R., Mason C. A., Ren K., Dijkstra M., Mesinger A., Pentericci L., Trenti M., Treu T., 2020, MNRAS, 495, 3602
Wilkins S. M., Lovell C. C., Stanway E. R., 2019, MNRAS, 490, 5359
Wise J. H., Abel T., 2008, ApJ, 685, 40
Wouthuysen S. A., 1952, AJ, 57, 31
Wu X., McQuinn M., Eisenstein D., Iršič V., 2021, MNRAS, 508, 2784
Wyithe J. S. B., Loeb A., 2013, MNRAS, 428, 2741
Xu H., Norman M. L., O'Shea B. W., Wise J. H., 2016a, ApJ, 823, 140
Xu H., Wise J. H., Norman M. L., Ahn K., O'Shea B. W., 2016b, ApJ, 833, 84
Yung L. Y. A., Somerville R. S., Finkelstein S. L., Popping G., Davé R., 2019, MNRAS, 483, 2983

APPENDIX A: STREAMING-VELOCITY SUPPRESSION ON THE MATTER POWER SPECTRUM

In this appendix we show a simple but accurate fit to the suppression on the small-scale matter power spectrum induced by the relative velocities.

Following Tseliakhovich & Hirata (2010) and Muñoz (2019a), we solve for the evolution of the DM and baryon densities for different initial values of v_{cb} and its inner-product cosine μ with each wavenumber k, in order to compute the density fluctuations of baryons and DM at each z and k. From there, we can calculate the matter power spectrum as a function of v_{cb} by averaging over μ, to find $P_m^2(k, z, v_{cb})$ (Tseliakhovich & Hirata 2010). We show in Fig. A1 the ratio of this quantity to its no-velocity counterpart

$$\mathcal{T}_m = \frac{P_m(k, z; v_{cb})}{P_m(k, z; 0)} \tag{A1}$$

as well as the fit defined in equation (14). The main feature of these curves is that larger values of v_{cb} produce a bigger drop in the power spectrum, as the larger relative velocity puts DM and baryons out of phase (or equivalently, it does not allow baryons to collapse to DM overdensities, slowing growth at small scales). However, at much smaller scales the baryonic fluctuations are damped due to the Jeans pressure, driving δ_b down for $k > k_J \approx 500$ Mpc^{-1}, and recovering the DM-only fluctuations regardless of v_{cb}. Put together, these two effect produce a dip at $k \approx 300$ Mpc^{-1} in Fig. A1, which turns back to unity at larger k.

We have used equation (14) to fit this dip as a Gaussian with three parameters (as described in Section 2 of the main text), where

$$\mathcal{T}_m(v_{cb}) = 1 - A_p \exp\left[-\frac{(\log[k/k_p])^2}{2\sigma_p^2},\right], \tag{A2}$$

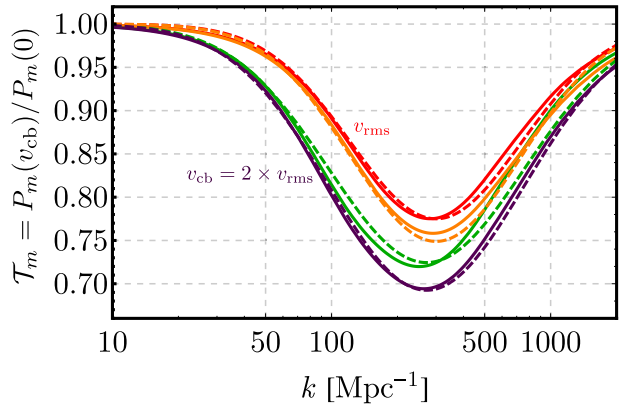

Figure A1. Transfer ratio of matter fluctuations at small scales due to the effect of the DM-baryon relative velocities v_{cb}, defined in equation (A1). The solid lines show the exact result from solving the ODEs (as in Muñoz 2019a), whereas the dashed lines show our Gaussian approximation from equation (A3). The red and green lines are evaluated at $z = 30$, whereas the orange and purple are at $z = 15$. Upper (red and orange) lines have $v_{cb} = v_{rms}$, whereas lower (purple and green) ones have $v_{cb} = 2 \times v_{rms}$. In the main text we use the $z = 20$ result, described in equation (14).

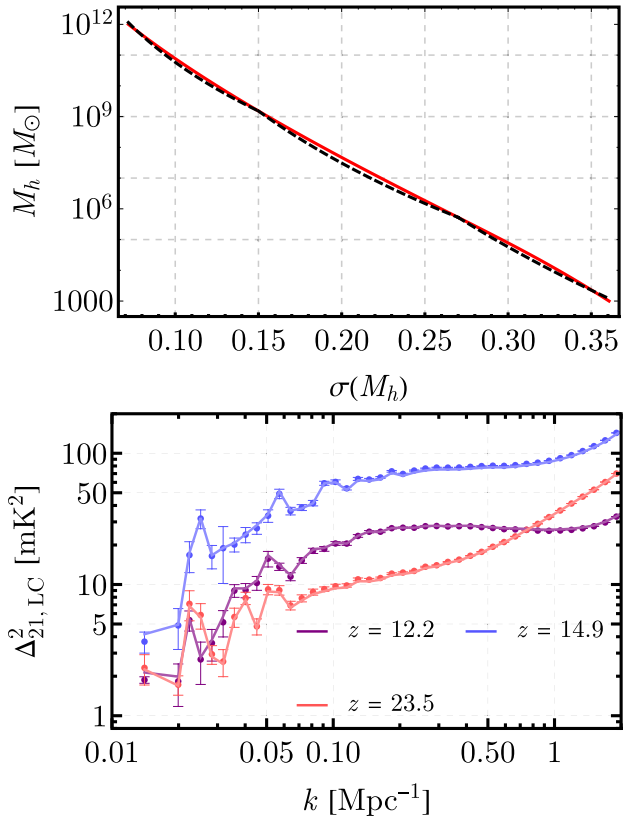

Figure A2. Top: Relation between the halo mass M_h and the rms fluctuation $\sigma(M_h)$ at their scales. The red line is the result using the full power spectrum, whereas the black dashed line is the broken power law from equation (B7). Note that we need to go to low M values (large σ) since in some cells $\delta_R \approx \delta_{crit}$, which corresponds to $\nu \to 0$ (or $\sigma \gg 1$). All σ are linearly extrapolated to $z = 0$. Bottom: Light-cone power spectra with the `FAST_FCOLL_TABLES` turned on (points with errors) and off (solid line) at three redshifts, for our OPT parameters. The difference between the two is negligible at high redshifts, and below 10 per cent at low redshifts. The global signal is identical to the percent level between the two cases.

and we find the following fits

$$A_p(v_{cb}, z) = 0.24 \times [(1+z)/21]^{-1/6} (v_{cb}/v_{rms})^{\alpha_p},$$
$$k_p(v_{cb}) = 300\,\mathrm{Mpc}^{-1} \exp[-0.2\ (v_{cb}/v_{rms} - 1)],$$
$$\sigma_p(v_{cb}) = 0.8(v_{cb}/v_{rms})^{1/3}, \quad \text{(A3)}$$

for the *Planck* 2018 cosmology, where $\alpha_p = 1$ for $v_{cb} \leq v_{rms}$ and $\alpha_p = 0.5$ otherwise. This heuristic fit was calibrated at $z = 20$, and while neither k_p nor σ_p depend on z we see it provides a good fit during the relevant z at cosmic dawn. To illustrate this point, we show the real transfer function $\mathcal{T}_m(v_{cb})$ in Fig. A1 at $z = 15$ and 30, as well as our fit, where the two are in good agreement.

APPENDIX B: FAST SFRD TABLES

The excursion-set algorithm in `21-cmFAST` takes advantage of the extended Press–Schechter approach (Bond et al. 1991) to find the SFRD (and its derived quantities such as the ionizating flux) at a given scale and overdensity. This requires tabulating the SFRD for many values of the overdensity δ_R and variance σ_R for different radii R, so as to not compute it in every cell at every z. This is not extremely computationally expensive for runs with only atomic-cooling galaxies (ACGs, taking approximately ∼2 min to generate the tables down to $z = 6$), though it is for runs with minihaloes hosting molecular-cooling galaxies (MCGs, taking ∼4 h for the same settings), as the tables ought to be generated for many different values of $M_{turn}^{(III)}$.

Here, we show an analytical approximation that allows us to compute those tables much faster, cutting the generation time of tables by a factor of ≈30.

In `21-cmFAST` the SFRD (and derived quantities such as UV and X-ray emissivities) is modulated using extended PS theory, where we have

$$\mathrm{SFRD}^{\mathrm{EPS}}(R, \mathbf{x}) \propto \int \mathrm{d}M_h \frac{\mathrm{d}n}{\mathrm{d}M_h}(\mathbf{x}) \dot{M}_*(M_h) f_{duty}(M_h), \quad \text{(B1)}$$

for each cell at $\mathbf{x}$ and radius R around it (which will enter an integral over previous times). The HMF depends on position through the overdensity $\delta_R(\mathbf{x})$ and the variance σ_R, and the pre-factor is

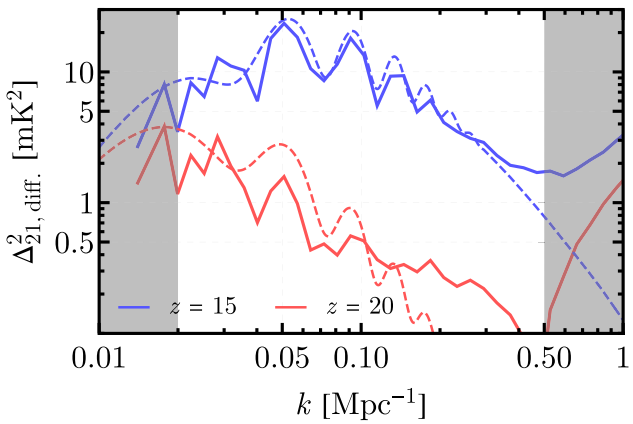

Figure B1. Difference between the full relative-velocity case and one with fixed $v_{cb} = v_{avg}$ (`FIX_VAVG` in the code), in solid blue at $z = 15$ and red at $z = 20$. These two cases have a similar background, but the VAOs are absent on the average case, as the velocities do not fluctuate. The dashed lines correspond to the fit from equation (27), with the biases and window functions from that section. We do not show error-bars on the simulation results here as it is the difference of two runs with the same initial conditions.

position-independent so it cancels out when dividing by the average over all cells. Our assumption is that feedback produces a power-law SHMR, equations (1), (7), so

$$\dot{M}_*(M_{\rm h}) \propto M_{\rm h} \times (M_{\rm h}/10^{10}\,{\rm M}_\odot)^{\alpha} \tag{B2}$$

for a power-law index α (which we can identify with α_* for X-ray and non-ionzing UV fluxes, but for ionizations is $\alpha = \alpha_* + \alpha_{\rm esc}$). In these calculations the HMF dn/dM is given by the standard old PS formula, as that is the only one for which the EPS formalism has been properly tested.

We will speed up the computation by using an approximate analytical solution. We know how to compute the integral in equation (B1) analytically for the case of $\alpha = 0$ (so $\dot{M}_*(M_{\rm h}) \propto M_{\rm h}$) with a sharp cutoff (i.e. a Heaviside rather than exponential functional form for $f_{\rm duty}(M_{\rm h})$). In that case we can use the variable $\nu = \delta^2_{\rm crit}/\sigma^2$ to re-write the integral as

$${\rm SFRD}^{\rm EPS}(\mathbf{x}, z) \propto \int_{\nu_{\rm min}}^{\infty} \frac{{\rm d}\nu}{\sqrt{\nu}} e^{-\nu/2} = \sqrt{2\pi}\,{\rm erfc}\left(\sqrt{\frac{\nu_{\rm min}}{2}}\right), \tag{B3}$$

where erfc is the complementary error function, and we have defined

$$\nu_{\rm min} = \delta^2_{\rm crit}/\sigma(M_{\rm turn})^2. \tag{B4}$$

The EPS formalism (Bond et al. 1991) shows that for regions of radius R that are overdense by δ_R, given a variance of matter fluctuations of σ_R^2, then all the ν are corrected to be $\tilde{\nu}$, defined as

$$\tilde{\nu} = \tilde{\delta}^2_{\rm crit}/\tilde{\sigma}^2, \tag{B5}$$

with $\tilde{\delta}_{\rm crit} = \delta_{\rm crit} - \delta_R$, and $\tilde{\sigma}^2 = \sigma^2 - \sigma_R^2$. This allows us to compute the SFRD at an arbitrary point through a simple erfc, as in equation (B3). This expression is exact, and extremely fast to evaluate (compared to performing many numerical integrals). So, while it cannot be used directly in our tables (as we do not have a Heaviside $f_{\rm duty}$ or $\alpha = 0$ always), it gives us a good scaffolding upon which to build our analytical solution.

First, we will use a Heaviside $f_{\rm duty}$ in our EPS, though we keep the usual (exponential) duty factor in the average result that normalizes at each z.

Secondly, we can use the following analytic integral,

$$\int_{\nu_{\rm min}}^{\infty} \frac{{\rm d}\nu}{\sqrt{\nu}} e^{-\nu/2} \nu^{\beta} = 2^{\beta+1/2}\Gamma\left(\beta + 1/2, \nu_{\rm min}/2\right), \tag{B6}$$

which is a generalization of equation (B3) adding a power-law ν^β. Then, the trick is to approximate the function

$$\sigma(M_{\rm h})/\sigma_{\rm p} = (M_{\rm h}/M_{\rm p})^{1/\gamma}, \tag{B7}$$

for some power-law index γ and pivot scale M_p (for which $\sigma(M_p) \equiv \sigma_p$). In practice, this can only be done over a small range of variances σ (or halo masses $M_{\rm h}$), as otherwise the functional form does not work. For LCDM models, and the mass range of interest, a good fit is a broken power law, with $\gamma = 9$ for masses below a first pivot ($M_{\rm h} < M_{p1} = 5.3 \times 10^5\,{\rm M}_\odot$), $\gamma = 21$ for masses above the second pivot ($M_{\rm h} > M_{p2} = 1.5 \times 10^9\,{\rm M}_\odot$), and where the index between the two pivots is set to $\gamma = 13.6$ by continuity. This approximates $\sigma(M_{\rm h})$ as a broken power law of $M_{\rm h}$ to ∼10 per cent precision, as shown in Fig. A2 which suffices for our purposes. For each of the power-law indices, we take $\beta = \alpha \times \gamma/2$ in equation (B6).

A subtletly is that for regions of radius R we will not just have a power law, but instead, following equation (B5) we will have

$${\rm SFRD}^{\rm EPS} \propto \int_{\nu_{\rm min}}^{\infty} \frac{{\rm d}\tilde{\nu}}{\sqrt{\tilde{\nu}}} e^{-\tilde{\nu}/2} \left(\nu/\nu_{\rm p}\right)^{\beta} \left(\frac{1}{1+\nu/\nu_{\rm p}}\right)^{\beta}, \tag{B8}$$

with $\nu_{\rm p} = \tilde{\delta}^2/\sigma^2$ (notice the lack of tilde on the σ^2 here). A further approximation is to break $(1+\nu/\nu_p)^{-\beta}$ into the two regimes of 1 and $(\nu/\nu_p)^{-\beta}$ for $\nu < \nu_p$ and $\nu > \nu_p$, respectively. Therefore, for $\nu \gg \nu_p$ the power laws cancel (recovering an erfc), whereas below it follows equation (B6). This allows us to write the collapsed fraction through this broken power law as a sum of Γ functions.

The code allows the user to turn on this functionality with the flag `FAST_FCOLL_TABLES`. By default they are not used for ACGs, as the speed boost is only ∼×2, but for MCGs it can reach × 30, so it is recommended. The calculation for the ionization tables proceeds identically, with $\alpha = \alpha_* + \alpha_{\rm esc}$. We show an example of how the SFRD compares to the exact calculation in Fig. A2, which for the MCG regime of interest agrees to ≈ 10 per cent, and ≈ few per cent for $\alpha = 0$, which is the MCG-assumed value. The agreement is even closer in practice, since we only use these tables for the EPS part of the calculation, so an overall offset is cancelled out, and only the δ behaviour remains. We note that we are not explicitly enforcing f_* or $f_{\rm esc}$ to be less than unity in these approximations. Although models that violate that condition are disfavoured by observations, we caution the reader to set off the `FAST_FCOLL_TABLES` when exploring a wide parameter space of extreme models.

APPENDIX C: VAOS WITHOUT POISSON NOISE

Here, we show a simple check that the VAOs can be recovered from our simulations with small Poisson variance. Our goal is to show that one need not run very large 21-cm boxes to obtain the large-scale VAOs, if two simulations are compared: one with full relative velocities and one with a fixed $v_{\rm cb} = v_{\rm avg}$. These two cases share a similar background evolution but have different large-scale power spectrum, as the $v_{\rm cb}$ anisotropies become imprinted on to the 21-cm fluctuations. We show the difference in the power spectra during the EoH and EoC in Fig. B1, as well as the fit we found in Section 5, which provides a reasonable approximation to this difference. Notice that the high-k part of the power spectrum still deviates in the two cases, as the background matching is not perfect for the average-velocity case. Subtracting these two cases severely reduces the simulation Poisson error (as the two simulations share initial conditions), though it does not fully cancel it, as clear from the data variation in Fig. B1. This helps extracting VAOs from more modestly sized simulations.

This paper has been typeset from a TEX/LATEX file prepared by the author.